









RESEARCH

Open Access



Engineering extracellular vesicles to transiently permeabilize the blood–brain barrier

Francesca Tomatis^{1,2,3} , Susana Rosa^{1,2} , Susana Simões^{1,2} , Marta Barão^{1,2,3} , Carlos Jesus^{1,2,9} , João Novo^{1,2,3} , Emanuel Barth^{4,5} , Manja Marz^{5,6,7,8}  and Lino Ferreira^{1,2,9*} 

Abstract

Background Drug delivery to the brain is challenging due to the restrict permeability of the blood brain barrier (BBB). Recent studies indicate that BBB permeability increases over time during physiological aging likely due to factors (including extracellular vesicles (EVs)) that exist in the bloodstream. Therefore, inspiration can be taken from aging to develop new strategies for the transient opening of the BBB for drug delivery to the brain.

Results Here, we evaluated the impact of small EVs (sEVs) enriched with microRNAs (miRNAs) overexpressed during aging, with the capacity to interfere transiently with the BBB. Initially, we investigated whether the miRNAs were overexpressed in sEVs collected from plasma of aged individuals. Next, we evaluated the opening properties of the miRNA-enriched sEVs in a static or dynamic (under flow) human in vitro BBB model. Our results showed that miR-383-3p-enriched sEVs significantly increased BBB permeability in a reversible manner by decreasing the expression of claudin 5, an important tight junction protein of brain endothelial cells (BECs) of the BBB, mediated in part by the knockdown of activating transcription factor 4 (ATF4).

Conclusions Our findings suggest that engineered sEVs have potential as a strategy for the temporary BBB opening, making it easier for drugs to reach the brain when injected into the bloodstream.

Keywords Extracellular vesicles, Modulation, MicroRNA, Blood–brain barrier, Microfluidic system, Claudin 5

*Correspondence:

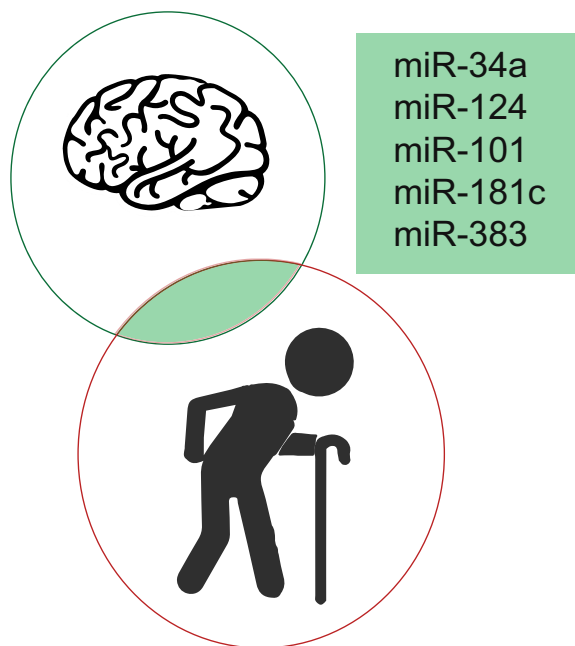
Lino Ferreira

lino.ferreira@uc.pt

Full list of author information is available at the end of the article



© The Author(s) 2024. **Open Access** This article is licensed under a Creative Commons Attribution-NonCommercial-NoDerivatives 4.0 International License, which permits any non-commercial use, sharing, distribution and reproduction in any medium or format, as long as you give appropriate credit to the original author(s) and the source, provide a link to the Creative Commons licence, and indicate if you modified the licensed material. You do not have permission under this licence to share adapted material derived from this article or parts of it. The images or other third party material in this article are included in the article's Creative Commons licence, unless indicated otherwise in a credit line to the material. If material is not included in the article's Creative Commons licence and your intended use is not permitted by statutory regulation or exceeds the permitted use, you will need to obtain permission directly from the copyright holder. To view a copy of this licence, visit <http://creativecommons.org/licenses/by-nc-nd/4.0/>.

Graphical abstract**Introduction**

The blood–brain barrier (BBB) is a physical and metabolic barrier that prevents undesired substances (e.g. pathogens) from reaching the brain. It is formed by endothelial cells (ECs) that interact with cells of the neurovascular unit (NVU), such as pericytes, astrocytes, and neurons [1]. This interaction contributes to the maintenance of the main brain ECs features such as a low pinocytotic activity [2], reduced transcytosis [3], a higher density of mitochondria [4], and tight junctions (TJs) proteins, contributing to a low permeability. Due to BBB organization only lipid soluble and smaller than 400 Da molecules are able to cross the biological barrier [5], representing a challenge for therapeutic delivery into the brain. This is particularly critical in the context of many brain diseases where the integrity of the BBB remains largely intact, thereby inhibiting the permeability of potential therapeutic drugs. Indeed, a high percentage of pre-clinical drugs identified for neurological disorders failed during the clinical trials due to their inability to cross the BBB [6, 7].

In recent years, several strategies have been investigated to transiently open the BBB to facilitate the delivery of drugs to the brain. The opening of the BBB can be induced by means of hyperosmotic solutions to induce an osmotic pressure (mannitol [8], arabinose, lactamide, urea [9]). It can also be obtained through chemical

agents, peptides and molecules with effects on the TJs (like sodium caprate [10], anti-netrin 1 antibody [11], histones [12]) or on receptors (gintonin [13] and RMP-7/Cereport [14]). Finally, the BBB opening can be induced with physical stimuli (focused ultrasounds and microbubbles [15, 16]; laser-induced thermal therapy [17], also coupled with gold nanoparticles [18, 19]; microbeam radiation therapy [20]), and RNA interference tools [21, 22]. The first to reach the clinic was the osmotic BBB disruption, used to deliver chemotherapeutics for brain tumor [23]. The intra-arterial administration of mannitol induced the shrinkage of BECs and the disruption of the TJs, allowing the crossing of molecules up to 20 nm for a 10 min period [24]. Yet, this approach might have some disadvantages since it generated a transient neuro-inflammatory response marked by increased production of cytokines and other biomolecules, leading to the activation of astrocytes, microglia, and macrophages [25]. In addition, the opening of the BBB by physical stimuli such as focused ultrasound coupled with microbubbles (the intervention being guided by magnetic resonance imaging) reached the clinical trials [26, 27]. This opening was reported to last 24 h and involved the disruption of the TJs, increase of vesicles and cytoplasmatic channels and formation of fenestrae [15]. The great advantage of this strategy is the spatial specificity but, even if in the clinical trials just mild adverse effects were observed,

the technique still presents some problems. First of all, inflammation and DNA damage were observed after using the focused ultrasounds [28], even if it was not clear if the cause of the cytokines increase was the mechanical effect of the microbubbles on the ECs (for example through the reduction of P-glycoprotein [29]) or the extravasation of blood-borne molecules. Secondly, due to the skull absorption of the ultrasound field and to the distinct susceptibility of different vessels, it is complicated to predict exactly the acoustic pressure on the area of interest [30], with the possibility to induce tissue damage. An FDA-approved molecule for cardiac therapy (Lexiscan, also known as Regadenoson) was also discovered to be able to induce the BBB opening for around 30 min [31]. This drug binds to the A2A adenosine receptor of the cells, and it reduces the expression of P-glycoprotein [32]. The *in vitro* results for the use of Lexiscan were promising; however, no efficacy was observed in patients when using the approved dose of the compound [33]. Overall, most of the strategies proposed until now have limitations, including side effects, and allow a limited control on the parameters for the BBB opening.

The BBB permeability increases during aging [34–36] and this can be an inspiration for the development of strategies to overcome the biological barrier. The BBB breakdown, determined by dynamic contrast-enhanced magnetic resonance imaging, is part of the normal aging process and occurs in the absence of neurological disorders [34, 35]. Inflammation is a key factor that can lead to both reversible and irreversible damage to the BBB. Acute inflammatory responses can cause temporary increases in permeability, while chronic or high levels of

inflammation may result in permanent BBB damage [37]. Importantly, blood components can regulate the permeability of the BBB and alter its “aging” phenotype. For example, young blood reverses age-related impairments in cognitive function and synaptic plasticity in aged mice [38]. In contrast, young mice administered with plasma from old mice showed decreased synaptic plasticity, impaired contextual fear conditioning and spatial learning and memory which indicates an impair in the BBB permeability [39]. It is likely, that part of this regulatory effect of the blood in the BBB is mediated by small extracellular vesicles (sEVs) [40]. sEVs are biological nanoparticles delimited by a lipid bilayer and containing several types of biomolecules, including non-coding RNAs [41–43]. They are secreted by most cell types, playing a key role in cell-to-cell communication and supporting both physiological and pathological processes. For example, sEVs isolated from the peripheral blood of aged mice and intravenously administered in young mice can pass the BBB and induce glial cell activation [44]. Yet, until now, it is relatively unknown (i) the interaction of blood EVs isolated from aged individuals or modulated with aging-related biomolecules, including non-coding RNAs, with the human BBB, (ii) if they can open the BBB and (iii) what is the mechanism.

Here, we have investigated *in vitro* the human BBB opening capacity of sEVs enriched with miRNAs that are overexpressed in sEVs collected from the plasma of aged human individuals (Fig. 1). To enrich the sEVs with the miRNAs we have used a protocol that has been recently reported by us that makes use of a chemical reagent to transfect the sEVs with miRNAs

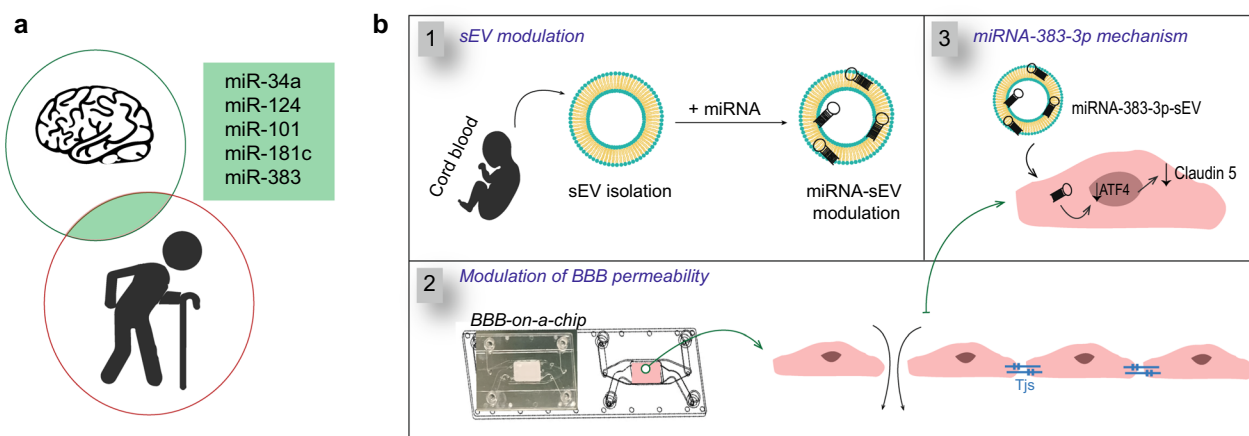


Fig. 1 Engineering extracellular vesicles to permeabilize the BBB. **a** Identification of the miRNA candidates that are simultaneously altered during aging or age-related diseases and have shown to affect BBB permeability. **b** Overview of the experimental setup. **b.1** sEVs collected from human UCB plasma were transfected with a miRNA of interest by a chemical agent. **b.2** MiRNA-enriched sEVs were tested in human *in vitro* BBB models both in static and flow conditions. **b.3** Identification of the mechanism behind the transient opening of the BBB after exposure to miRNA-enriched sEVs

[45]. We have evaluated the BBB opening properties of 4 miRNA-enriched sEVs formulations in a static and then one of those in a dynamic (using microfluidics) human in vitro BBB model (Fig. 1). To the best of our knowledge, this study identifies for the first time a sEV-enriched formulation able to transiently open the BBB, both in static and dynamic human BBB models, inspired by physiological aging. Importantly, this work was performed in human in vitro models that have been previously validated to predict CNS distribution of compounds in humans [46]. It is aligned with the European Union goals on the protection of animals used for scientific purposes based on replacement, reduction, and refinement (3Rs).

Materials and methods

Isolation of sEVs

The blood samples were diluted 1:1 in dilution buffer (phosphate-buffered saline (PBS) with 2 mM of EDTA) to improve the efficiency of the process. The plasma was separated from the whole blood by using density gradient medium Lymphoprep™ (STEMCELL Technologies, ref. 07861) and centrifugation (400g at 20 °C, 35 min) without breaks. The plasma was then collected and frozen at – 80 °C until usage.

sEVs were isolated from UCB plasma (“young EVs”) and plasma from adult donors between 58 and 64 years old (“old EVs”, Fig. 2b). In both cases, the plasma was centrifuged (2000g, 20 min) to remove possible cells and cell

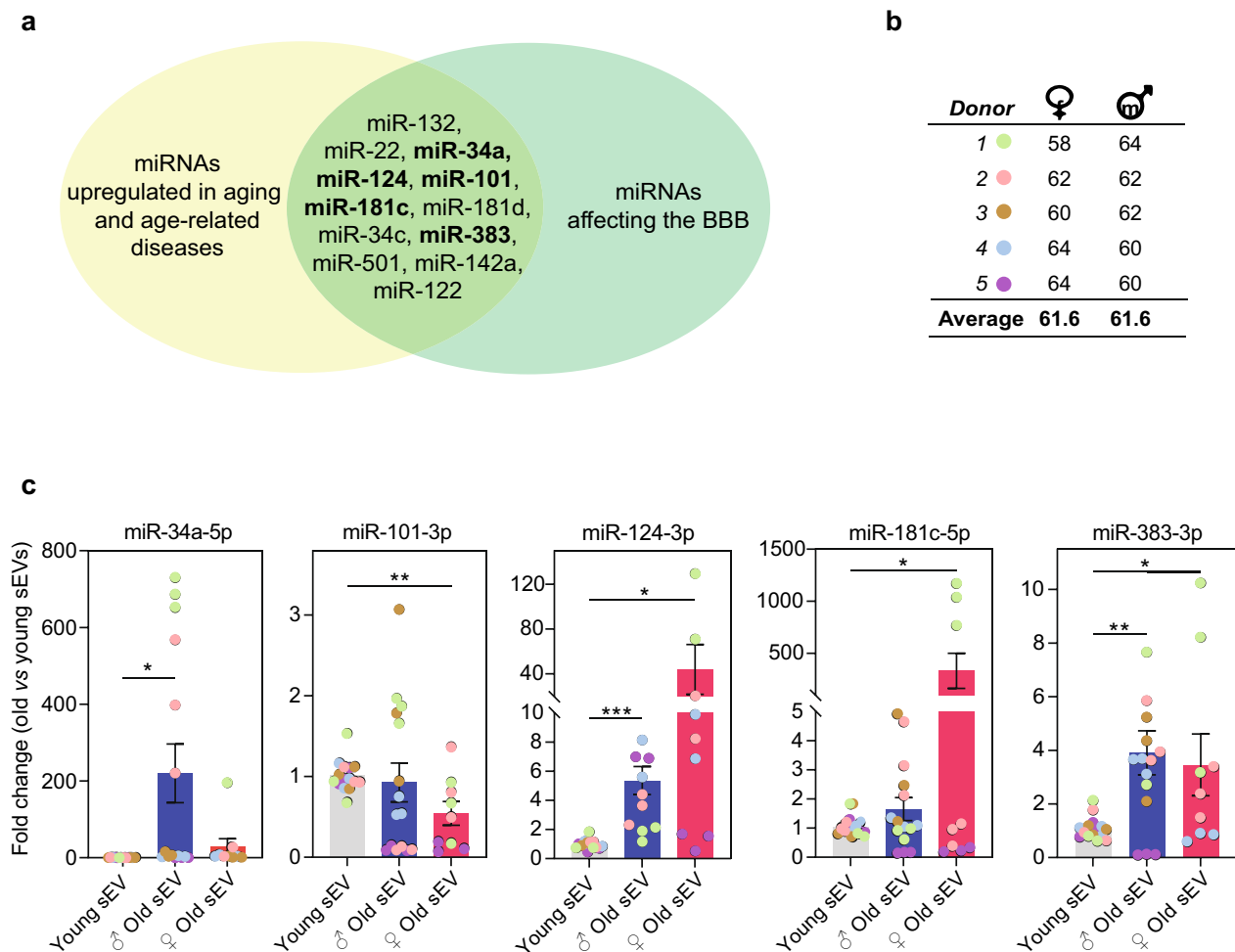


Fig. 2 Expression of miRNAs in sEVs changes during aging. **a** Scheme representing the list of miRNAs (in bold) selected for our study. **b** Table with the ages of the adult plasma donors (expressed in years old). For both males and females, the average is 61.6 years old. **c** RT-qPCR analyses performed to characterize the miRNA content in sEVs from plasma of aged donors (aged 58–64; labeled as “old sEVs”) compared to the sEVs from umbilical cord blood (UCB, labeled as “young sEVs”). Five miRNAs were evaluated. The data are expressed as mean \pm SEM, $n=5$ biological samples (2–3 technical replicates per biological sample). The unpaired t -test statistical analysis was performed for each miRNA, comparing the young sEVs with old sEVs from male and female donors. The * means $p < 0.05$, ** means $p < 0.01$, *** means $p < 0.001$

debris before moving to the ultracentrifugation steps. Microvesicles and apoptotic bodies were removed with 2 centrifugations (10,000g, 30 min each). Then the vesicles were separated through ultracentrifugation (100,000g, 2 h). The obtained sEVs were passed through size exclusion columns (qEVoriginal 35 nm from IZON, ref. SP5) to remove the proteins from the samples. Before size exclusion chromatography purification, an aliquot was collected for protein quantification using micro-BCA protein assay kit (Thermo Scientific, ref. 23235). Finally, the sEVs were concentrated by centrifugation (100,000g, 2 h) and they were stored in aliquots at -80°C . The ultracentrifugation was carried out in an Optima XPN 100K ultracentrifuge (Beckman Coulter, CA, USA) equipped with a swinging bucket rotor SW 32 Ti and 28.7 mL polyallomer conical tubes (Beckman Coulter).

Preparation of miRNA-enriched sEVs

sEVs from UCB plasma were transfected with Exo-Fect Exosome Transfection Kit (SystemBiosciences, ref. EXFT20A-1), following manufacturer's instruction with some optimization. Briefly, 1.5×10^{11} sEVs in PBS were mixed with 904 pmol of miRNA (miRIDIAN microRNA Mimic, Horizon) and 10 μL of Exo-Fect in a total volume of 150 μL . A scrambled miRNA was used as negative control for the experiments (from now on called "miR-scr"). Then, the sample was incubated at 37°C for 10 min at 350 rpm. In order to purify the sEVs from the excess of Exo-Fect and miRNA, the vesicles were added on top of an Optiprep density gradient (ODG) composed of 4 layers of iodixanol at 40%, 20%, 10% and 5% (each layer of 8 mL) in non-conical polyallomer tubes, as previously reported [47]. In order to create the layers, the Optiprep (stock solution at 60%) was diluted to a working solution of 50% by using the working buffer (0.25 M sucrose, 6 mM EDTA, 60 mM Tris-HCl, pH=7.4) and the right percentages were obtained by adding the proper amount of homogenization buffer (0.25 M sucrose, 1 mM EDTA, 10 mM Tris-HCl, pH=7.4). The ODG was centrifuged (100,000g, 18 h) and fractions of 4 mL were collected, numbering them from 1 to 8 from top to bottom. The fractions from 3 to 6 contained the modulated sEVs (density ranging between 1.04 and 1.12 g/mL), so they were collected and diluted in PBS. Then, the sEVs were collected by ultracentrifugation (100,000g, 2 h). They were stored at 4°C and used in the following 2 days, without freezing them.

Characterization of sEVs: dynamic light scattering (DLS)

The size and charge of sEVs was characterized by DLS. For each batch, 4×10^9 sEVs were analyzed. sEVs were diluted in molecular grade water. Both size and zeta potential were measured by averaging at least 3 runs per

each sample. At least 3 different sEVs isolations per condition were analyzed. The DLS analysis was carried out with ZetaPALS zeta potential analyzer from Brookhaven Instruments Corp.

Characterization of sEVs: nanoparticle tracking analysis (NTA)

The size and concentration of sEVs was characterized by NTA using NanoSight NS300 (Malvern Instruments, UK). The process involved manual injection of the sample at a flow rate of approximately 1 mL every 20 s. The sEVs were diluted in PBS to obtain a concentration between 15 and 45 particles per frame. Five 30-s videos were recorded for each sample, using a camera level of 15. The videos were analyzed using NTA 3.4 analytical software, with the threshold set between 4 and 5 based on the quality of the videos.

Characterization of sEVs: TEM analysis

For the TEM analysis of sEVs, the samples were mixed with an equal volume of 4% paraformaldehyde (PFA) (1:1 v/v) and placed on formvar-carbon coated copper grids (Micro To Nano, ref. 22-1MFC) for a 5 min room temperature incubation. After removing the material in excess, the grids were incubated for 1 min with a solution of uranyl acetate 2% in water. sEVs images were obtained using a Tecnai G2 Spirit BioTWIN electron microscope at 100 kV.

Characterization of sEVs and ECs: miRNAs expression analyses

RNA was extracted from 1.4×10^{11} UCB/old vesicles, 1.0×10^{10} modulated vesicles (and corresponding native) or from approximately 1×10^5 ECs (co-cultured with pericytes on the Transwell[®] system for 6 days) with the miRNeasy Micro kit (Qiagen, ref. 217084) accordingly to the manufacturer instructions. The cDNA synthesis was done with the miRCURY LNA RT kit (Exiqon, ref. 339340). Then, 10 ng of extracted RNA were used for the cDNA synthesis. Reverse transcription quantitative polymerase chain reaction (RT-qPCR) was performed by employing miRCURY LNA miRNA PCR Assay (Qiagen, ref. 339306). For the RT-qPCR, a 30 times dilution of cDNA was performed, and 3 μL were loaded per well. RT-qPCR was done using the CFX Connect Real-Time System (Bio-rad, CA, USA). For each qPCR experiment, qPCR reactions were performed in triplicate. Relative levels of mRNA were normalized to the level of house-keeping gene (U6 small nuclear RNA). The sequences of primers from Qiagen (U6 snRNA ref. YP00203907, hsa-miR-34a-5p ref. YP00204486, hsa-miR-383-3p ref. YP02108841, hsa-miR-101-3p ref. YP00204786) and

Exiqon (hsa-miR-181c-5p ref. 204683, hsa-miR-124-3p ref. 206026) are proprietary.

Characterization of sEVs: western blot analyses

Western blot analyses were performed to detect markers of EVs (CD9, CD63, Alix, GAPDH) and contaminants (calnexin) in sEV preparations. Samples of sEVs isolated from UCB, from plasma of old donors (Donor 1: male 64 years old; Donor 2: female 64 years old) and from modulated sEVs were analyzed. For the analysis of sEVs contaminants, CD34⁺ ECs (P5) were lysed in RIPA buffer (EMD Millipore Corporation, ref. 20–188) supplemented with protease/phosphatase inhibitor cocktail (Cell Signaling, ref. 5872). Cell lysates were centrifuged (20,000g, 10 min at 4 °C) and supernatants transferred to a new tube and immediately stored at – 80 °C until use. Total protein was quantified with the micro-BCA protein assay kit (Thermo Scientific, ref. 23235). For each sample, 4 µg of protein extract were mixed with 10 µL of 5×Laemmli buffer (0.35 M Tris–HCl at pH 6.8, 10% SDS, 30% glycerol, 0.6 M DTT—dithiothreitol, 0.012% bromophenol blue) and Milli-Q water to reach 50 µL. No reducing agents were used in the samples to analyze tetraspanins. The samples were denaturated (95 °C, 5 min), then loaded in the stacking gel (4% acrylamide bisacrylamide, 126 mM Tris–HCl at pH 6.8, 0.1% SDS, 0.1% TEMED, 0.05% ammonium persulfate) and resolved in a running gel (12% acrylamide bisacrylamide, 375 mM Tris–HCl at pH 8.8, 0.1% SDS, 0.05% TEMED, 0.05% ammonium persulfate). Gel electrophoresis was carried out in a running buffer (25 mM Tris, 192 mM glycine, 0.1% SDS, pH 8.3) using a voltage of 80 V for 30 min to allow the samples to enter and cross the stacking gel and then moving to 120 V for 45 min for the resolving gel. The electrophoresis was performed with the EV265 power supply from Consort.

The proteins in the gel were electrotransferred into a PVDF membrane (Amersham™ Hybond™ 0.45 PVDF membranes; Cytiva, ref. 10600023), previously activated in methanol, in wet conditions at 100 V for 90 min on ice (EV265 power supply device, Consort). The membranes were then blocked for 1 h at room temperature (RT) in 5% BSA in TBS-T (Tris-buffered saline, 0.1% Tween 20). Primary antibodies were diluted in 1% BSA in TBS-T and incubated overnight at 4 °C. The list of the antibodies with the used dilutions is reported in Additional file 5: Table S4. The day after, the membranes were washed 3 times with 1% (w/v) BSA in TBS-T for 5 min and then incubated for 1 h at RT with secondary antibody (Additional file 5: Table S4). Finally, the membranes were washed 3 times with 1% BSA in TBS-T. The protein detection was accomplished by a chemiluminescence reaction using WesternBright Quantum and

WesternBright Peroxide HRP substrate parts 1 and 2 (Advansta, ref. R-03026-B35 and ref. R-03025-B35). The chemiluminescent signal was visualized in the Imager from VWR International BVBA and VWR Image capture software.

In vitro BBB model: preparation

Human brain vascular pericytes (HBVP, ScienCell, sc-1200) and human endothelial cells (ECs) differentiated from CD34⁺ cells [46] collected from UCB were used. Pericytes were seeded in 12 multiwell plates pre-coated with 2 µg/cm² poly-L-lysine (PLL) in sterile water for 1 h at 37 °C (ScienCell, SC-0413) at a density of 4200 cells/cm² in pericyte medium (ScienCell, sc-1202). Six hours after, ECs were seeded (80,000 cells/insert) in Transwell®-Clear Inserts with Polyester (PET) membrane (Corning, 3460) or Transwell® permeable supports with polycarbonate membrane (Corning, 3401) previously coated with Matrigel™ (Basement Membrane Matrix, 10 mL *LDEV-Free, BD) diluted 1:48 in cold Dulbecco's Modified Eagle's Medium (DMEM) for 1 h at room temperature (RT). The co-culture was maintained in Endothelial Cell Growth Medium-2 BulletKit™ (EGM-2, Lonza, CC-3162) supplemented with 1 ng/mL of human basic fibroblast growth factor (hbFGF, Sigma, F0291) with medium changes every other day [46]. Modulated sEVs (0.5 mL at 10¹⁰ sEVs/mL if not otherwise specified) were added on day 4 in serum EVs-depleted EGM2 by 18 h of centrifugation at 100,000g. Both pericytes and ECs were used until passage 6.

In vitro BBB model: trans-endothelial electrical resistance (TEER) characterization

The plates with the Transwell® systems were kept at RT for 10 min before starting the measurements. TEER was measured using a Millicell ERS-2 Epithelial Volt-Ohm Meter (ref. MERS00002M, Merck Millipore, Darmstadt, Germany). TEER readings of cell-free inserts were subtracted from the values obtained with cells. The results obtained were multiplied by the area of the insert membrane (1.12 cm²) as previously reported [46]. For each experiment the results were normalized relative to the control condition.

In vitro BBB model: permeability to lucifer yellow

The paracellular permeability was evaluated as previously described [46], through a lucifer yellow (LY) assay. Briefly, HEPES-buffered Ringer's solution (1.5 mL; NaCl 8.8 g/L, KCl 0.387 g/L, CaCl₂ 0.244 g/L, MgCl₂ 6H₂O 0.0406 g/L, NaHCO₃ 0.504 g/L, HEPES 1.19 g/L, glucose 0.504 g/L, pH=7.4) was added to each well of a 12 well plate (Costar, ref. 3737). The Transwell® inserts, with or without the monolayer of brain ECs (BECs), were added to the

top and the culture medium was replaced with 500 μL of 20 μM LY (Sigma, ref. L 0259) in Ringer's buffer. The plate was left in the incubator at 37 $^{\circ}\text{C}$ for 60 min, and every 20 min the bottom compartment of the filter without cells (used to calculate the cleared volume in the absence of the barrier) was changed in order not to reach equilibrium. After 1 h, the solutions from top and bottom compartments were collected and the fluorescence (excitation wavelength 430 nm, emission wavelength 530 nm) was measured in black 96 multiwell plates (Costar, ref. 3915) in Synergy H1 microplate reader (Bio Tek). The clearance principle was employed to obtain transport results independent of the concentration [46].

In vitro BBB model: cell viability assay

To assess ECs viability, cells were incubated with PrestoBlue (Invitrogen, ref. A13261) diluted 10 times in EGM2 medium for 30 min. After that period, the solution was collected, and fluorescence was measured in a black 96 multiwell plate (excitation wavelength 560 nm, emission wavelength 590 nm) in a Synergy H1 microplate reader (Bio Tek). For the calculations, the blank value obtained from PrestoBlue incubation without cells was subtracted. For each experiment the results were expressed relative to the respective control.

In vitro BBB model: flow cytometry

BECs were brought to cell suspension using 0.05% trypsin for 5 min at 37 $^{\circ}\text{C}$. Each condition analyzed was performed in duplicate. Cells were centrifuged at 300g for 5 min, resuspended in PBS with 10% FBS and counted. Fixation was performed with 1% PFA for 10 min at room temperature, cells were centrifuged at 500g for 5 min to remove PFA and washed once with PBS with 10% FBS, followed by another centrifugation step. BECs were permeabilized with 0.1% Triton for 5 min, centrifuged (500g \times 5 min) and incubated with 5 μL (each condition) of anti-Claudin 5 antibody (FITC) (Biorbyt, orb400830) for 1 h at room temperature in PBS with 10% FBS. After cells were washed 2 times in PBS and resuspended in 300 μL of PBS before analysis in BD LSRFortessaTM flow cytometer. Data analysis was performed with FLOWJO software.

In vitro BBB model: mRNA expression by RT-qPCR

BECs were lysed after 6 days of co-culture (around 100,000 cells) with RLT lysis buffer (350 μL ; Qiagen, ref. 1053393) and RNA was extracted with RNeasy Plus Micro Kit (Qiagen, ref. 74034). RNA concentration was measured with NanoDropTM 2000 Spectrophotometer (Thermo Scientific). cDNA synthesis was done from 500 ng of RNA in a 10 μL reaction using qScript cDNA SuperMix (Quanta BioSciences, ref. 95048). Afterwards,

cDNA samples were diluted to 2.5 ng/ μL . RT-qPCR was done with 5 ng of cDNA per each reaction using NZY Speedy qPCR Green Master Mix (nzytech, ref. MB224) and a thermocycler CFX Connect Real-Time System (Bio-rad, CA, USA). qPCR reactions in triplicate were performed for each qPCR experiment. Relative levels of mRNA were normalized to the reference gene β -actin and analyzed with the $\Delta\Delta\text{Ct}$ method. The sequences of the primers used, bought from Sigma or from IDT, are reported in Additional file 5: Table S5.

The putative direct target genes of miR-383-3p were found both in the literature (*ATF4* [48], *RAB4A*, *PTEN* and *MFSD2A* [3, 49], *NR3C2* [50]) and in databases such as miRDB (<https://mirdb.org>) and TargetScan (<https://www.targetscan.org>) (*NRP1/NELL1*, *ZBTB34*, *SEC61A1*, *STX16*, *ZNF354B*, *JARID2*, *MED28*, *AEN*, *ZMAT4*, *CLASPI*, *DHX33*).

Vybrant-DiO sEVs labelling

sEVs were incubated for 20 min at room temperature with VybrantTM DiO Cell-Labeling Solution (Invitrogen, ref. V22886) at a proportion of 1.5 μL of dye to each 100 μL of sEVs. Then, labelled sEVs were purified by SEC technique and concentrated by ultracentrifugation at 100,000g for 2 h, 4 $^{\circ}\text{C}$. As negative control of the staining, the protocol was replicated without the presence of sEVs (including SEC purification and ultracentrifugation concentration).

Immunocytochemistry

ECs were fixed either with PFA 4% (v/v) for 10 min or ice-cold methanol: acetone (1:1) for 2 min (Additional file 5: Table S6). Cells were washed with PBS 3 times. The cells fixed in PFA were permeabilized with 0.1% (v/v) Triton-X 100 (Sigma) for 10 min except for CD31 staining (internalization experiments), where permeabilization was omitted to avoid the destruction of the sEVs. Cells were washed with PBS 3 times and blocked with 5% (w/v) BSA for 1 h at RT. The membranes were cut from the Transwell[®] support and split according to the number of staining's desired. The primary antibodies (Additional file 5: Table S6) were diluted in Antibody Diluent with Background Reducing Components (DAKO, ref. S3022) and were incubated overnight at 4 $^{\circ}\text{C}$. On the following day, cells were washed 3 times with PBS and then incubated with the secondary antibody (Additional file 5: Table S7) for 1 h at RT. After PBS washes, the cells were counter-stained with DAPI (2 $\mu\text{g}/\text{mL}$, 10 min). Finally, the insert membranes were mounted on glass slides with Vectashield fluorescence mounting medium (Vector Laboratories, ref. H-1400) and z-stack images were taken with laser scanning confocal microscope (LSM 710, Zeiss) with a 40 \times objective.

BBB-on-a-chip model

The BBB-on-a-chip was developed by us and contained ECs cultured in the top compartment of an Organ-on-a-Chip Cross flow membrane—Mini Luer 0.2 μm (Darwin Microfluidics, ref. CS-10000737) and human pericytes in the bottom compartment. Both cells were perfused with cell culture medium, that in the upper channel was pumped by an IBIDI pump system (IBIDI, ref. 10902). The coating of the channels was performed as described for the static BBB model, but PLL concentration was increased to 3 $\mu\text{g}/\text{cm}^2$ and both coatings were incubated at 37 °C due to the impossibility to separate the channels from each other. Pericytes were seeded on the bottom channel of the chip (50,000 cells in 70 μL , 42,000 cells/ cm^2), while CD34⁺ ECs were seeded on the upper channel on top of the membrane (150,000 cells in 90 μL , 97,000 cells/ cm^2). One day after the seeding, the culture medium was changed. On day 2 after seeding, the microfluidic chip was connected to the IBIDI pump (IBIDI red perfusion set, ref. 10962). The flow rate was increased every 15 min in 6 steps from 2 mL/min to 13.3 mL/min, equivalent to 4 dyn/ cm^2 in the central area of the chip with the membrane. The cells were maintained in these conditions until day 6. For the experiments with sEVs, on day 6 the flow was stopped, the perfusion system was changed (IBIDI yellow perfusion set, ref. 10965) and then the microfluidic chip was connected to the IBIDI pump for additional 24 h, with a flow rate of 0.3 mL/min, equivalent to 0.1 dyn/ cm^2 . The permeability to LY was determined as described for the static BBB model, but a higher LY concentration was used (200 μM) and the incubation period was decreased to 30 min. The assay was performed in static conditions. At the end of the assay (30 min), 90 μL were collected from the top channel (and diluted 1:10) and 70 μL were collected from the bottom one (and diluted 1:5), and the fluorescence intensity was measured.

Statistical analysis

Data in the figures are expressed as mean \pm SEM. For multiple comparisons, * p < 0.05, ** p < 0.01, *** p < 0.001. Unpaired t-test or one-way ANOVA followed by Tukey's multiple comparison test were performed, depending on the number of conditions to compare. Two-way ANOVA statistical analysis was performed, followed by Sidak's multiple comparison test, for the temporary effect analysis data.

Results

Expression of miRNAs in plasma sEVs during aging

Initially, we checked different studies to find miRNAs that were altered during aging or age-related diseases, both in human and murine samples of EVs, plasma and

blood [51–72]. We have identified 615 miRNAs that were upregulated during aging and 131 miRNAs that were upregulated in age-related diseases (Additional file 2: Table S1). Next, we have identified 36 miRNAs that have been described to affect the BBB permeability (Additional file 3: Table S2) [73–109]. The miRNAs whose mechanism of action at the BBB involved apoptosis were excluded from the list. Finally, we intersected the two lists to find miRNAs that were regulated during aging or age-related diseases and at the same time reported to affect the BBB (Fig. 2a). We found 12 miRNAs (miR-132-3p, miR-22-3p, miR-34a, miR-124-3p, miR-101-3p, miR-181c-5p, miR-181d-5p, miR-34c, miR-383, miR-501-3p, miR-142a-3p, miR-122-5p) (Additional file 4: Table S3) from which we selected 5 (miR-34a-5p, miR-181c-5p, miR124-3p, miR-101-3p, miR-383-3p) for further analyses, based in their potency (e.g. miR-34a-5p, miR-181c-5p, miR124-3p) and little information about their mechanism (e.g. miR-383-3p, miR-101-3p).

To demonstrate that the miRNAs identified were indeed upregulated during aging, we characterized their presence in sEVs isolated from plasma of human UCB (“young sEVs”) or plasma from adult individuals without medical pathologies (between 58 and 64 years old; “old sEVs”) (Fig. 2b). In both cases, the sEVs were initially isolated by ultracentrifugation and further purified by size exclusion chromatography (SEC). SEC reduced the protein content in sEVs by approximately 99.6%, leading to a 38.8-fold increase in EV purity (Additional file 1: Figure S1a–d). Furthermore, the results indicate that the mean and mode sizes of sEVs remained unchanged following the purification process. The old sEVs were similar, in terms of size and charge, compared to the young sEVs (Additional file 1: Figure S2a–e), but they had a statistically higher content of proteins (Additional file 1: Figure S2f). Western blot results showed the presence of tetraspanins (CD9 and CD63) and Alix in both young and old sEVs (Additional file 1: Figure S2g). The results further show that EVs do not show the presence of contaminant markers such as calnexin, an endoplasmic reticulum protein present in cells, which confirms their purity (Additional file 1: Figure S2g). All the miRNAs were found to be overexpressed in sEVs collected from the plasma of old individuals compared to young sEVs, except miR-101-3p (Fig. 2c). However, this can be explained with the fact that this miRNA was reported to be upregulated in pathological (age-related disease) and not during physiological aging [63, 64, 72]. In addition, we observed an upregulation of miR-383-3p in old sEVs (Fig. 2c), which was not reported previously during physiological aging (only in stroke models [67]). Interestingly, for miR-34a-5p, miR-181c-5p, and miR-124-3p we found a marked difference in their expression levels accordingly to the gender of

the donors. This aspect warrants further investigation in the near future, as it aligns with other studies indicating a gender bias in the miRNA content of sEVs in various contexts [110, 111]. Altogether, 4 over 5 of the miRNAs tested were overexpressed in sEVs collected from aged individuals and were further investigated.

Preparation and characterization of miRNA-enriched sEVs

To deliver the miRNAs in the BBB, we used sEVs from UCB plasma. We have selected this sEVs because they are (i) easy to isolate from biological samples collected in a non-invasive way before UCB cells cryopreservation, (ii) sEVs from plasma have shown to interact easily with the BBB [110], and (iii) they don't raise immunological issues during allogenic transplantations [111]. sEVs were enriched with the miRNAs by a chemical transfection agent (Exo-Fect) previously reported by us to be effective to load miRNAs on sEVs [45]. The protocol for the sEVs enrichment with miRNAs included a transfection step and a purification step by ultracentrifugation using an Optiprep density gradient (ODG), followed by the sEVs concentration by ultracentrifugation (Fig. 3a). UCB-sEVs before ("native") and after miRNAs enrichment ("modulated") were characterized. The modulated sEVs maintain the protein expression of the native sEVs markers CD63 and CD9 (Fig. 3b). NTA measurements showed that the majority of both native and modulated sEVs had a size between 100 and 120 nm (Fig. 3c). TEM analysis showed slightly smaller diameters compared to the ones measured with NTA. The size distribution of the samples ranged between 75 and 100 nm (Fig. 3d, e) and was similar between native and modulated sEVs. The size of the samples measured through the DLS was larger than what showed by the previous results. However, also in this case no significant differences were observed between the native sEVs (184 ± 49 nm) and the modulated ones (174 ± 16 nm) (Fig. 3f). Concerning the z-potential, the two groups of samples showed values in the same range: -31 ± 2.2 mV for the native sEVs and -35 ± 1.5 mV for

the modulated sEVs (Fig. 3g). To confirm the enrichment of sEVs with miRNAs, RT-qPCR analyses were performed in native and miRNA-enriched sEVs. Our results showed an enrichment of more than 10^6 -fold in sEVs for each miRNA tested (Fig. 3h). The level of miRNA concentration in modulated sEVs (Fig. 3h) is much higher than the one observed for the same miRNAs in "old" sEVs (Fig. 2c). In order to better understand the meaning of these results, we also checked the basal expression level of each one of the miRNAs considered in the sEVs, compared to the expression of U6 (Fig. 3i). Overall, sEVs were enriched for miRNAs of interest and their morphological and charge properties were similar to the native counterparts.

Capacity of miRNA-enriched sEVs to permeabilize a human BBB model

To test the activity of the enriched sEVs, in vitro models can be used to reduce ethical concerns regarding animal experiments and to improve relevance to human physiology. To investigate the impact of the enriched sEVs to overcome a biological barrier, a human BBB co-culture model was used [46]. In this model, brain ECs expressed typical ECs cell markers such as MCAM gene (Additional file 1: Figure S7a) as well as claudin 5, claudin 1, occludin, ZO-1, JAM-A proteins [46]. Initially, we evaluated whether native sEVs, i.e. non-modified with miRNAs, would affect the properties of an in vitro human BBB model, such as BECs TEER and paracellular permeability to LY. For these tests, we exposed the in vitro BBB model to different concentrations of native sEVs (0.5 mL per filter at the concentrations of 2.4×10^9 , 10×10^9 or 16×10^9 sEVs/mL, for a final total number of sEVs per BBB model equal to 1.2×10^9 , 5×10^9 or 8×10^9) for 48 h. The time-point was selected according to previous studies [84]. The results obtained for TEER and paracellular permeability of LY showed that native sEVs did not interfere with the BBB properties (Additional file 1: Figure S3a, b). Importantly, the non-responsiveness of the BBB model to

(See figure on next page.)

Fig. 3 Modulation of sEVs with miRNAs. **a** Schematic representation of the sEV modulation protocol. The loading of miRNAs on the sEVs (904 pmol of miRNA per 1.5×10^{11} sEVs) was performed with Exo-Fect™ reagent followed by the ODG purification and ultracentrifugation to remove the excess of miRNA and Exo-Fect™. **b** CD63 and CD9 protein expression in both native and modulated-sEVs ($n = 2$ independent experiments). **c** NTA characterization of the native and the modulated sEVs (each curve represents the average of 3 independent sEVs isolations). **d** Representative TEM images of the native sEVs and of the modulated miR-383-3p-sEVs. Scale bar = 100 nm. **e** The diameter frequency of the native and modulated-sEVs. The results represent the quantification of 8–10 images of each condition, measuring more than 300 sEVs per condition using the ImageJ software. **f** The size and **g** zeta potential of native sEVs and modulated miR-383-3p-sEVs measured by Dynamic Light Scattering. The results are expressed as mean \pm SEM ($n = 3$ independent experiments with 1–3 technical replicates). **h** RT-qPCR quantification of three miRNAs (miR-181c-5p, miR-383-3p and miR-34a-5p) in modulated sEVs normalized by the amount of miRNAs in the native sEVs. Data are expressed as mean \pm SEM ($n = 3$ independent experiments; 3 technical replicates per independent experiment). **i** Basal expression of the miRNAs in the young native sEVs compared to the expression of housekeeping U6 small nuclear RNA by RT-qPCR analyses. Results are expressed as mean \pm SEM ($n = 5$ independent experiments with 3 technical replicates)

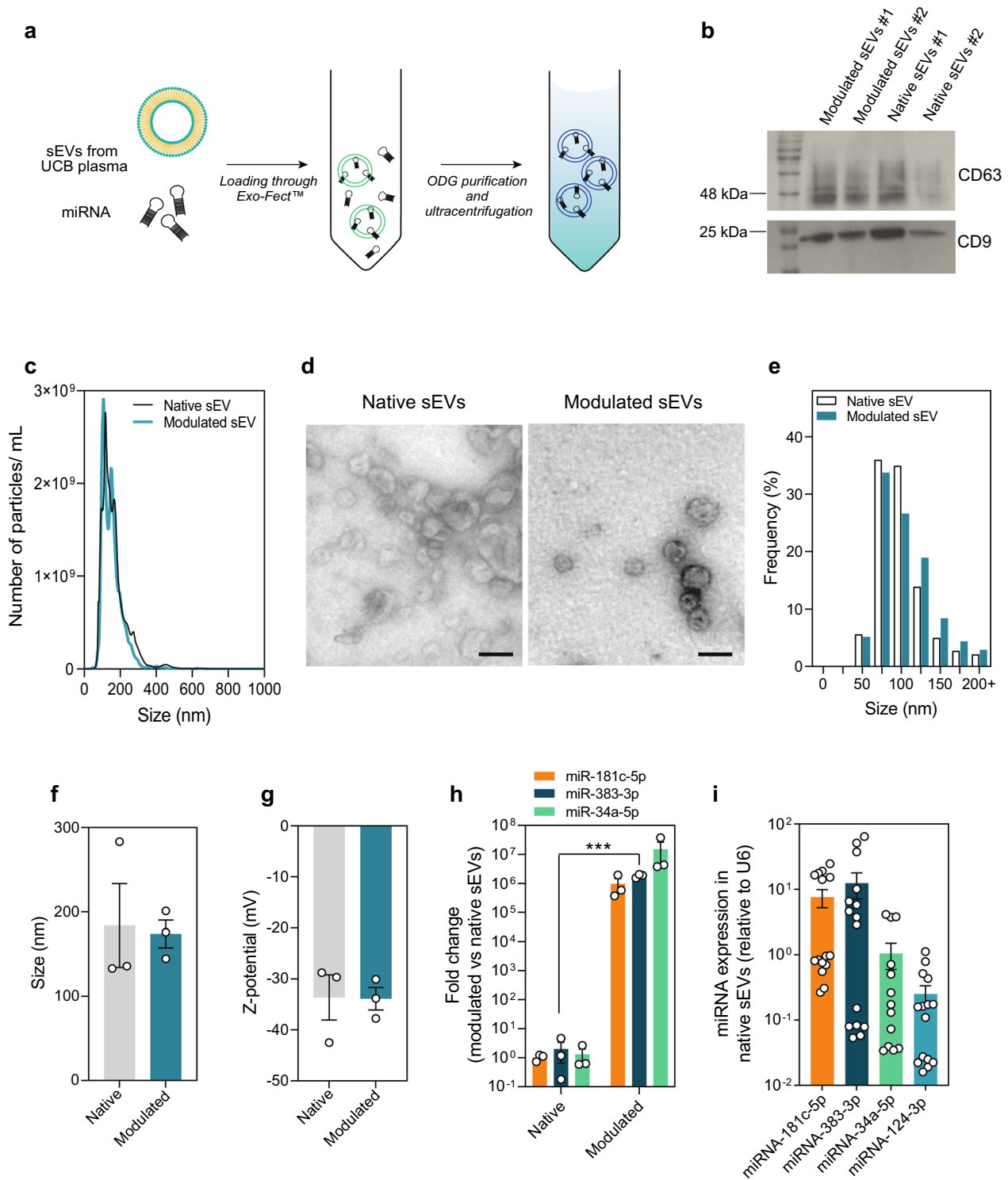


Fig. 3 (See legend on previous page.)

native sEVs was not due to a low capacity of the model to respond to extrinsic factors. Indeed, the exposure of the BBB model to TNF α (10 ng/mL, 24 h) halved the TEER values and doubled the paracellular permeability to LY

(Additional file 1: Figure S3c, d), confirming the responsiveness of our BBB model.

To investigate the internalization of the sEVs, ECs of the BBB model were incubated with 0.5 mL of medium

with Vybrant-DiO labelled-sEVs (native and scramble miRNA-enriched sEVs) at a concentration of 5×10^9 sEVs per BBB model. Medium containing free Vybrant-DiO dye, but not sEVs, processed in the same way as for native and scramble miRNA-enriched sEVs, was used as negative control following the MISEV2023 Guidelines [112] (Additional file 1: Figure S3e). After 24 h, the fluorescence intensity of the cells was measured. As expected, no fluorescence was observed in the negative control group indicating that Vybrant-DiO dye did not form nanostructures able to confound the interpretation of the results. Importantly, fluorescence intensity was similar between BECs incubated with native and scramble miRNA modulated sEVs, suggesting that sEV enrichment process did not affect internalization (Additional file 1: Figure S3e, f).

To evaluate the effect of miRNA-enriched sEVs in the BBB model (Fig. 4a), we initially quantified the basal expression of the four miRNAs in BECs (Fig. 4b). From the analyzed miRNAs, miR-383-3p and miR-124-3p were the ones with the lowest expression levels relative to the reference gene U6. Next, the BECs monolayer integrity was evaluated 48 h after the incubation with sEVs enriched with miR-34a-5p, miR-181c-5p, miR-124-3p or miR-383-3p. sEVs enriched with miR-181c-5p, miR-124-3p or miR-383-3p induced a statistically significant increase in the BBB model permeability to LY (Fig. 4c), a decrease in the BBB model TEER (Fig. 4d), and a variable impact in BEC viability (Fig. 4e), as compared to control sEVs (miR-scr-sEVs). The effect of sEVs enriched with miR-383-3p on paracellular permeability was somewhat greater than that observed with other modulated sEVs; therefore, it was selected for further analysis in subsequent experiments. Preliminary tests indicated that ECs transfected with RNAiMAX lipofectamine complexed with miR-383-3p exhibited increased paracellular permeability to LY compared to those transfected with miR-scr

(Additional file 1: Figure S4). The choice to base miRNA selection on paracellular permeability results, rather than on TEER measurements, is supported by the understanding that TEER values can be influenced by several variables—such as temperature changes and operator differences—that may undermine their reliability. In contrast, paracellular permeability assays offer a more consistent assessment.

To study the mechanisms by which miR-383-3p-sEVs induced a higher BBB permeability, the expression of TJ proteins (claudin 5, ZO-1 and occludin) as well as vWF, an endothelial marker, was analyzed at mRNA (Fig. 4f) and protein level, by both immunofluorescence (Fig. 4g, h) and flow cytometry (Additional file 1: Figure S5) analyses. At the protein level (immunofluorescence analyses), while ZO-1 and occludin expression remained similar in BECs incubated with miR-383-3p-sEVs or miR-scr-sEVs, there was a statistically significant decrease in the expression of claudin 5 in BECs incubated with miR-383-3p-sEVs ($55\% \pm 8\%$) as compared to miR-scr-sEVs (Fig. 4g, h). A significant decrease of claudin 5 (ca. 40%) was also monitored by flow cytometry analyses (Additional file 1: Figure S5). In contrast, there was an increase (although not statistically significant) in the expression of vWF in cells incubated with the miR-383-3p-sEVs as compared to cells incubated with miR-scr-sEVs. Importantly, the alterations observed at protein level for claudin 5, ZO-1, vWF, or occludin were not observed at gene level indicating that the observed effects were mediated by the intracellular delivery of the miRNA (Fig. 4f). Overall, our results showed that miR-383-3p-sEVs (i) were internalized by BECs at levels similar to native sEVs, (ii) induced a significant increase in the BBB model permeability to LY, (iii) induced a significant decrease in the BBB model TEER, and (iv) decreased the expression of the TJ protein claudin 5 in BECs while leading to the accumulation of vWF.

(See figure on next page.)

Fig. 4 Impact of miR-enriched-sEVs in the static human in vitro BBB model. **a** Schematic representation of the experimental setup. The BBB phenotype was established through 4 days of co-culture in Transwell systems. The modulated sEVs (10^{10} sEVs/mL) were incubated for 48 h with the BECs, then the medium was replaced with fresh medium and the ECs monolayer integrity was evaluated through TEER, paracellular permeability and cell viability. **b** Basal expression of the miRNAs used for the sEVs modulation in the BECs. Values are mean \pm SEM ($n = 3$ independent experiment with 3 technical replicates). **c** Paracellular permeability (Pe) to Lucifer yellow (LY), **d** TEER values and **e** BEC viability after 48 h of incubation with miR-enriched sEVs. Cell viability was assessed by a PrestoBlue assay. The values are normalized to the respective controls (miR-scr-sEVs) and expressed as mean \pm SEM, $n = 2-4$ independent experiments with 3 technical replicates (each experiment with a different batch of sEVs, therefore 3 different donors). Unpaired t test between each condition and the BBB model incubated with the miR-scr-sEVs was performed as statistical analysis. *, **, and *** denote statistical significance ($p < 0.05$, $p < 0.01$, $p < 0.001$). **f** Gene expression analysis of claudin 5, ZO-1, vWF, and occludin in BECs after 48 h incubation with 10^{10} miR-383-3p-sEVs/mL. The results are mean \pm SEM, $n = 4$ independent experiments with 3 technical replicates. **g** Representative confocal images of claudin 5, ZO-1, β -catenin, occludin, and vWF after the incubation with the miR-scr-sEVs and with miR-383-3p-sEVs. Scale bar is 20 μ m. **h** Mean intensity of the immunostaining for claudin 5, ZO-1, β -catenin, occludin, and vWF after incubation with miR-enriched sEVs. The values were normalized by miR-scr-sEVs condition. The data are mean \pm SEM, $n = 3-6$ independent experiments with 2-4 images per experiment. Statistical analysis was performed with an unpaired student's *t*-test, *** $p < 0.001$

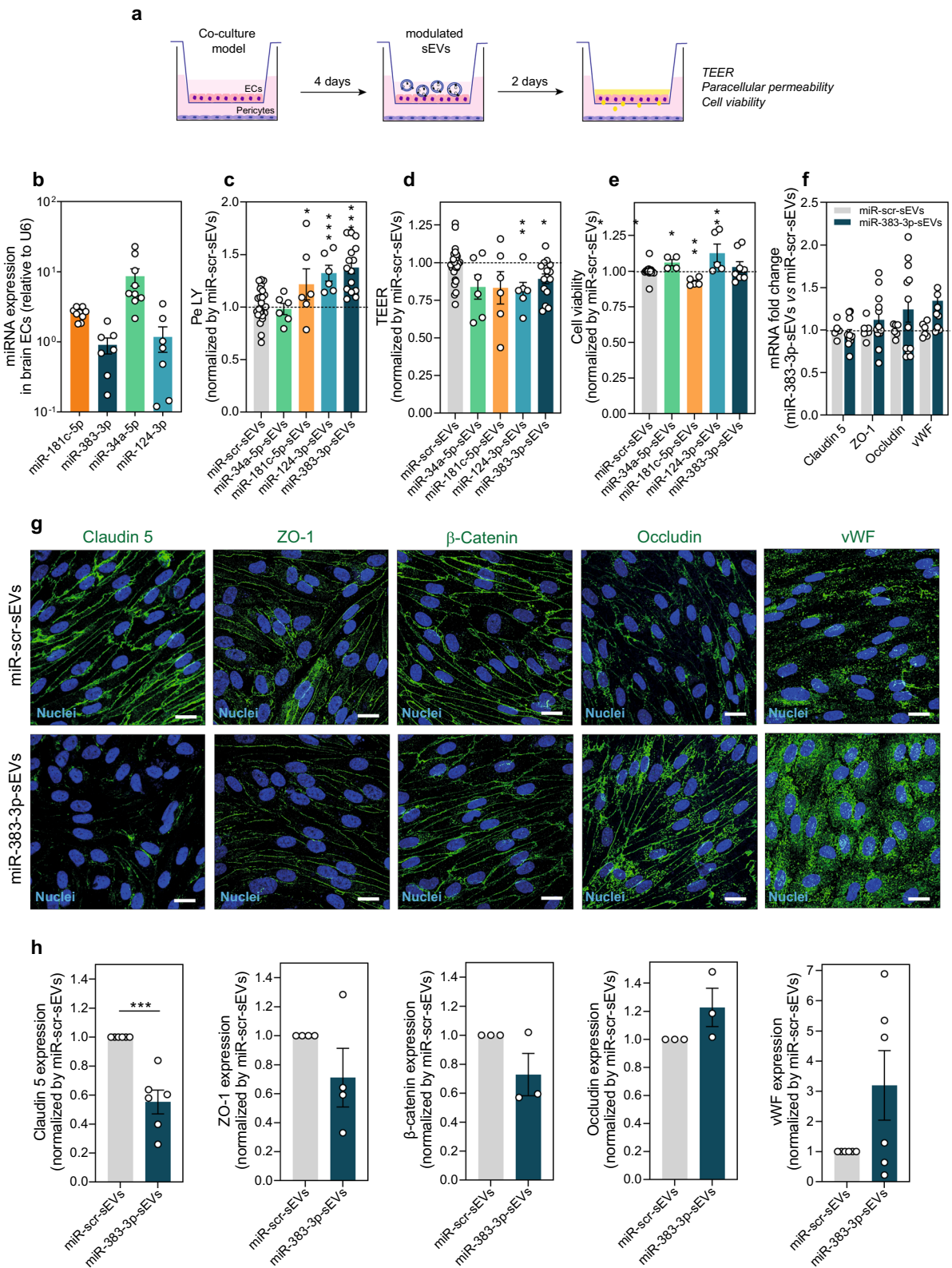


Fig. 4 (See legend on previous page.)

Time course of the BBB permeabilization

To investigate if the BBB permeabilization induced by miR-383-3p-sEVs was temporary, BBB TEER and BBB permeability to LY were evaluated at day 6 of co-culture (after 48 h of incubation with modulated sEVs) and again at day 7 (24 h after removing the miR-383-3p-sEVs) (Fig. 5a). At day 6, a significant increase of the permeability was observed in BECs incubated with miR-383-3p-sEVs ($128\% \pm 7\%$) (Fig. 5b) compared to the condition with miR-scr-sEVs, while at day 7 no difference was noticed between the two conditions (Fig. 5b) ($99\% \pm 16\%$ for the miR-383-3p-sEVs compared to miR-scr-sEVs). The alterations in TEER were less evident between the

two times but the trend was similar (Fig. 5c). Importantly, at day 7, the decrease in the BBB permeability was correlated with an increase in claudin 5 expression in BECs (Fig. 5d, e). In conclusion, our results indicate that the increase in the BBB permeability is temporary, recovering at the baseline levels after 24 h.

Mechanism of the BBB permeabilization

To understand the mechanism by which miR-383-3p-sEVs induced the opening of the BBB, we performed RT-qPCR analyses in BECs after incubation with miR-383-3p-sEVs for several genes reported in databases or in the literature as miR-383-3p targets (*ATF4*, *NR3C2*,

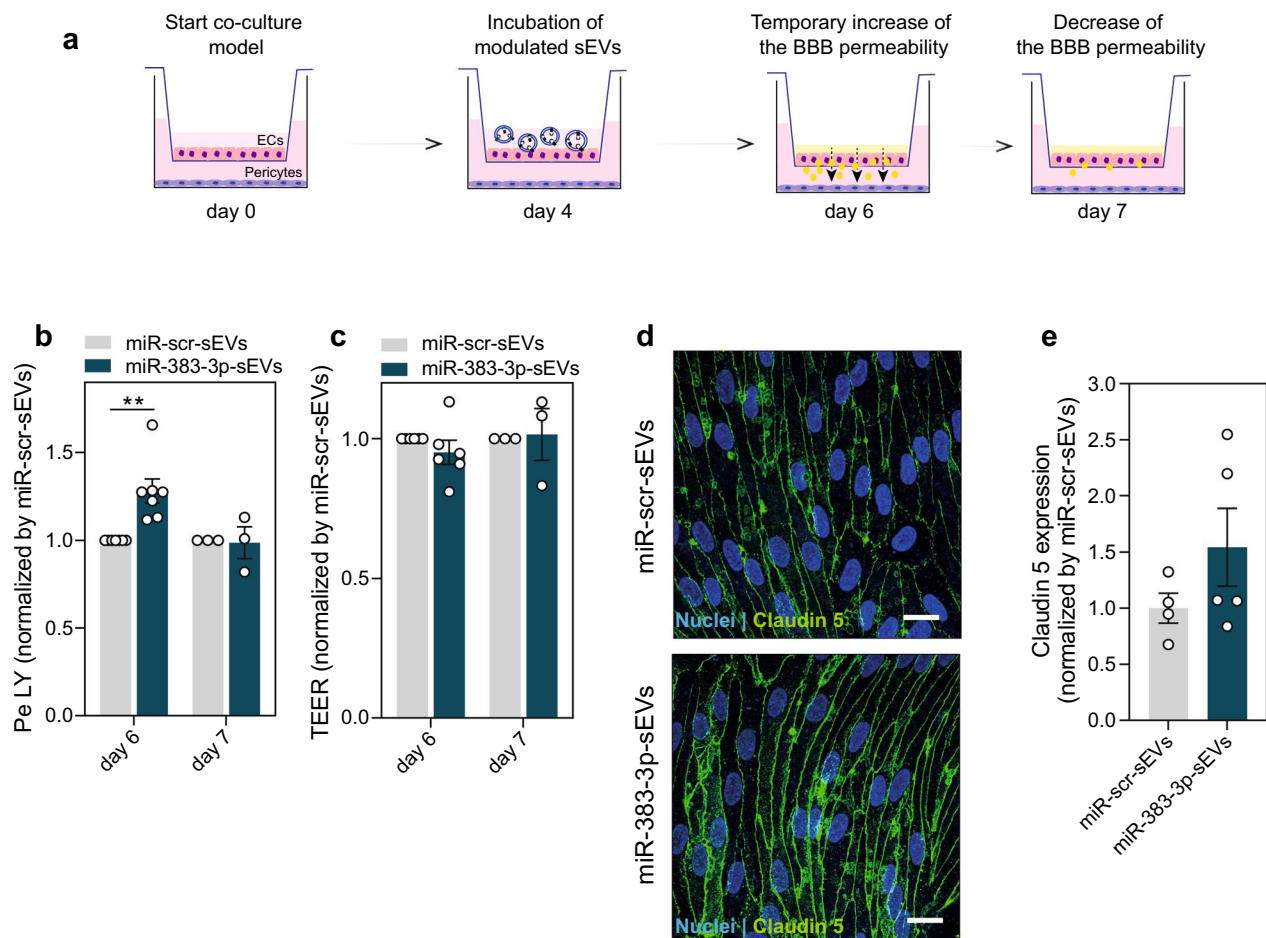


Fig. 5 Temporary effect of the miR-383-3p-enriched-sEVs on the BBB opening. **a** Schematic representation of the experimental protocol.

The miR-383-3p-enriched-sEVs (10^{10} sEVs/mL) were added to the upper compartment of the BBB model at day 4. After 48 h (day 6) the TEER and the paracellular permeability were measured. After the removal of the sEVs suspension, the BBB model was cultured with fresh medium for more 24 h (day 7), and monolayer integrity was evaluated. **b** Paracellular permeability to LY and **c** TEER values at day 6 and day 7. Results are expressed as mean \pm SEM, $n = 3$ –7 independent experiment with 3 technical replicates. Two-way ANOVA statistical analysis was performed, followed by Sidak's multiple comparison test, ** means $p < 0.01$. **d** Representative confocal images of claudin 5 at day 7. The BBB model was exposed to miR-383-3p-sEVs and to miR-scr-sEVs for 24 h. Scale bar is 20 μm . **e** Quantification of the mean fluorescence intensity of claudin 5. Results are expressed as mean \pm SEM, $n = 3$ independent Transwells systems, with 1–3 images per experiment. Unpaired t-test statistical analysis was performed ($p = 0.226$).

ZBTB34, *SEC61A1*, *STX16*, *ZNF354B*, *JARID2*, *MED28*, *AEN*, *ZMAT4*, *CLASP1*, *DHX33*, *NRP1*, *RAB4A*, *PTEN*, *MFSD2A*) (see Materials and Methods section).

Although the expression of some of the analyzed genes was significantly different between BECs incubated with miR-383-3p-sEVs and miR-scr-sEVs (Additional file 1: Figure S6), the only two genes that were significantly decreased in the condition with miR-383-3p-sEVs

were *ATF4* ($29\% \pm 7\%$) (Fig. 6a) and *NR3C2* ($32\% \pm 4\%$) (Fig. 6f). *NR3C2* upregulation has been linked to a higher release of vWF from the ECs [50], therefore its knock-down through miR-383-3p-sEVs could decrease the vWF release and explain its accumulation in the cells (Fig. 4h). Moreover, BECs grown with an excess of vWF were proven to express less claudin 5 compared to the control BECs [113], leading to an increased BBB permeability.

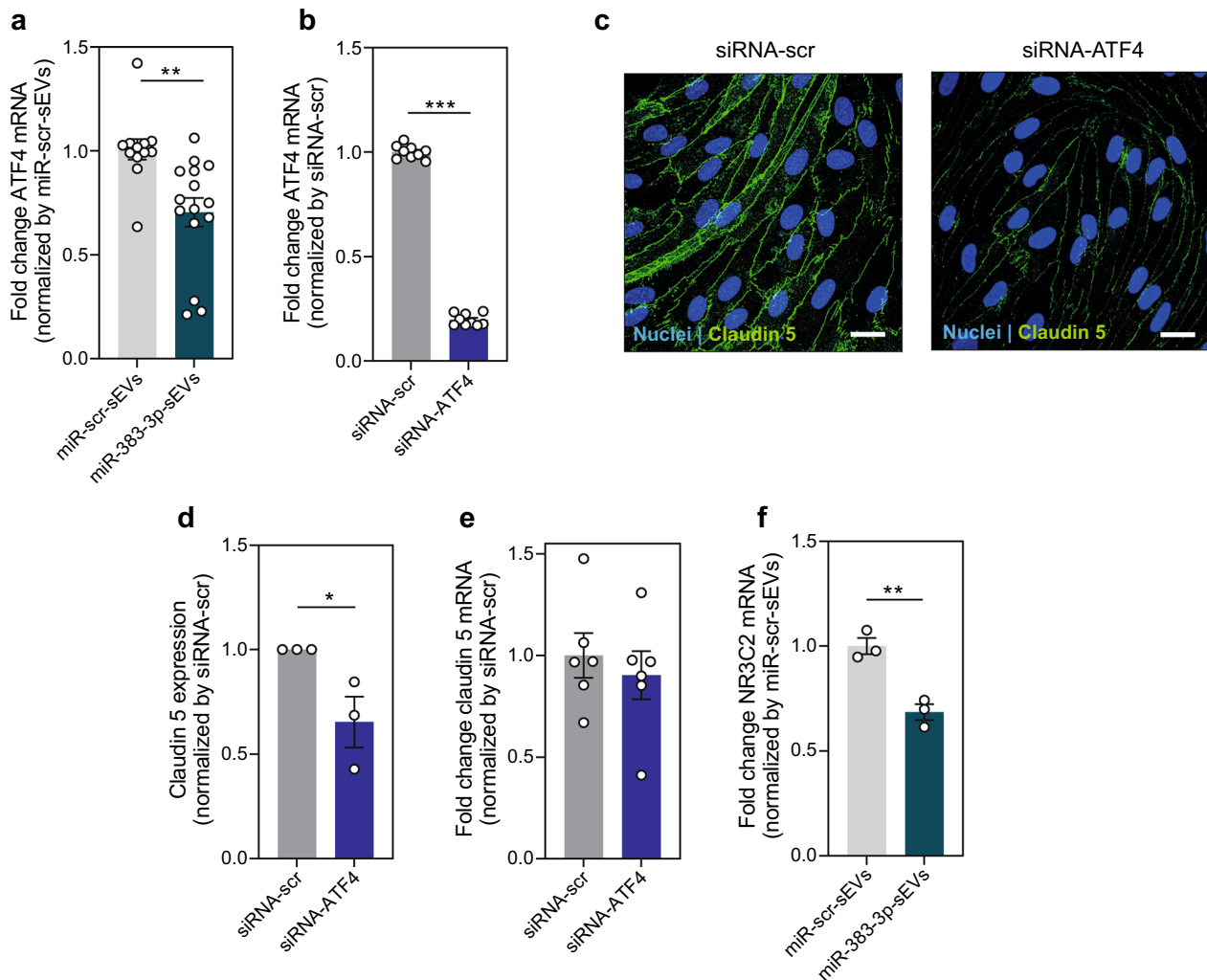


Fig. 6 Mechanism behind BBB opening after transfection with miR-383-3p-enriched sEVs. **a** ATF4 mRNA expression in brain ECs after 48 h of the incubation with miRNA-scr-sEVs or miRNA-383-3p-sEVs (both at 10^{10} sEVs/mL) in a static BBB model. Results are expressed as mean \pm SEM, $n = 5$ independent experiments with 3 technical replicates. **b** ATF4 mRNA expression in brain ECs after transfection with siRNA-ATF4. The brain ECs were transfected with siRNA-ATF4 (50 nM) or siRNA scramble control (siRNA-scr, 50 nM) using lipofectamine RNAiMAX as transfection agent, for 48 h. Values are expressed as mean \pm SEM, $n = 3$ independent experiments with 3 technical replicates. **c** Representative confocal images of claudin 5 immunostaining for brain ECs incubated with siRNA-ATF4 or siRNA-scr. Scale bar is 20 μ m. **d** Quantification of claudin 5 protein expression in brain ECs after transfection with siRNA-ATF4. The results were normalized by siRNA-scr. Results are expressed as mean \pm SEM, $n = 3$ independent experiments with 3 images per sample in each experiment. **e** Quantification of claudin 5 mRNA expression in brain ECs transfected with siRNA-ATF4 or siRNA-scr for 48 h. β -actin was used as reference gene. Results are expressed as mean \pm SEM, $n = 2$ independent experiments with 3 technical replicates. **f** Quantification of NR3C2 mRNA expression in brain ECs 48 h after transfection with miR-383-3p-enriched-sEVs or miR-scr-enriched-sEVs. β -actin was used as reference gene. Results are expressed as mean \pm SEM, $n = 3$ technical replicates. In **(a)**, **(b)**, **(d)** and **(f)** statistical analyses were performed using an unpaired t -test; * $p < 0.05$, ** $p < 0.01$, *** $p < 0.001$

Our results further show that miR-383-3p-sEVs had minor or no effect in the activation of inflammatory genes such as VCAM1 and ICAM1 in ECs, at least in the conditions and times tested (Additional file 1: Figure S7). To evaluate whether the decrease in *ATF4* mRNA levels could be related with the decrease of claudin 5 at the protein level, we transfected BECs with an *ATF4*-targeting siRNA (control cells were incubated with a siRNA negative control, “siRNA-scr”). siRNA-*ATF4* transfection induced a significant decrease in *ATF4* mRNA levels ($80\% \pm 1\%$) (Fig. 6b) and in claudin 5 protein level assessed by immunofluorescence compared to the condition with siRNA-scr ($35\% \pm 12\%$ compared to the siRNA-scr condition) (Fig. 6c, d). However, it did not affect the claudin 5 mRNA expression (Fig. 6e). Overall, our results showed that miR-383-3p-sEVs induced the opening of the BBB by targeting NR3C2 and ATF4 genes, which in turn controlled directly or indirectly the expression of claudin 5 protein.

Effect of miR-383-3p-sEVs on a human BBB-on-a-chip

BBB-on-chip technologies are important to better mimic the physiology of the human BBB [114]. Different BBB-on-a-chip models, with different configurations and perfused with media at different shear stresses (between 4 [115] and 6 dyn/cm^2 [116]), have been developed mostly based on normal human brain microvascular endothelial cells [116], immortalized human BECs, such as hCMEC/D3 [115], and human BECs isolated from iPSCs [117, 118]. Importantly, very few BBB-on-a-chip models have been used to evaluate the permeability of sEVs [119], and so far, none has been used to evaluate the permeabilization effect of modulated sEVs. Here, to evaluate the permeabilization properties of miR-383-3p-sEVs in conditions that resemble more closely to the human physiology, we have developed a human BBB model in a microfluidic chip under the effect of flow shear stress (4 dyn/cm^2) (Fig. 7a). The microfluidic chip

is commercially available and formed by two chambers separated by a poly(ethylene terephthalate) membrane ($12 \mu\text{m}$ thick, with $0.2 \mu\text{m}$ diameter pores, density of $1 \times 10^5 \text{ pores/cm}^2$) coated by us with a poly-L-lysine solution. Human ECs derived from cord blood hematopoietic progenitor cells (CD34^+ cells) [46] were plated in the luminal compartment of the microchip and maintained in co-culture with human pericytes (abluminal compartment) (Fig. 7a, b) to induce BBB formation. In the first 2 days, ECs were left in static conditions to allow them to reach the confluency. At this stage, ECs show less organized expression of claudin 5 than at day 6 (after 4 days under flow) (Fig. 7c, d). By another hand, the permeability to LY decreased from $3.7 \times 10^{-3} \pm 0.9 \times 10^{-3} \text{ cm/min}$ at day 2 to $2.1 \times 10^{-3} \pm 0.3 \times 10^{-3} \text{ cm/min}$ at day 6 (Fig. 7e). In addition, the ECs after 4 days under flow developed more organized TJ's claudin 5 (Fig. 7c), which together with lower LY permeability values suggest ECs specification into BBB phenotype (from now on termed as BECs).

Next, the internalization of VybrantDiO-labelled sEVs by BECs cultured under static and flow conditions, was investigated at time 24 h. When VybrantDiO-EVs were incubated in the presence of flow, the internalization was significantly lower compared to the sEVs incubated in static conditions. The internalization was measured as the total fluorescence intensity of VybrantDiO-sEVs, divided by the total number of cells by condition (Fig. 7f, g). Despite the lower levels of internalization of sEVs in the BBB-on-a-chip as compared to the static BBB model, when incubating it with miR-383-3p-sEVs for 24 h under flow we observed an average 0.4-fold increase in the permeability to LY of the dynamic model in comparison with the condition incubated with miR-scr-sEVs (Fig. 7h). Similar to the static BBB model we found decreased levels of claudin 5 protein and increased vWF expression in BECs incubated with miR-383-3p-sEVs compared to the cells incubated with miR-scr-sEVs (Fig. 7i, j, l). We then investigated whether this level of permeability could also

(See figure on next page.)

Fig. 7 Impact of miR-383-3p-enriched-sEVs in a human BBB-on-a-chip model. **a** BBB-on-a-chip coupled to IBIDI pumps. **b** Scheme of the BBB-on-a-chip: ECs ($97,000 \text{ cells/cm}^2$) seeded in the luminal compartment, pericytes ($42,000 \text{ cells/cm}^2$) in the bottom channel. After 2 days in static conditions, shear stress (4 dyn/cm^2) was added to BECs for 4 days. **c** Representative confocal images of claudin 5 at day 2 (static) and at day 6 (flow). Scale bar is $20 \mu\text{m}$. **d** Quantification of claudin 5 area in BECs. Results are mean \pm SEM ($n=2$ independent experiments, 4–5 images per system). Unpaired *t* test was performed, $**p < 0.01$. **e** Pe to LY in flow conditions checked every day until day 6 after cells seeding. Results are mean \pm SEM, $n=3$ –6 independent experiments, with 1–2 technical replicates. **f** Representative confocal images for the internalization of VybrantDiO-labelled sEVs (10^{10} sEVs/mL) in static and flow (0.1 dyn/cm^2) conditions 24 h after incubation. Scale bar is $20 \mu\text{m}$. **g** Mean fluorescence intensity of the Vybrant-DiO-sEVs per cell. Results are mean \pm SEM ($n=2$ independent experiments, 4–5 images for each membrane). Unpaired *t* test was performed, $***p < 0.001$. **h** Pe of the BBB 24 h after incubation with miR-scr-sEVs or miR-383-3p-sEVs (10^{10} sEVs/mL) with a shear stress of 0.1 dyn/cm^2 . Results are mean \pm SEM ($n=3$ independent experiments). Unpaired *t* test statistical analysis was performed, $*p < 0.05$. **i** Representative confocal images of claudin 5 and vWF expression in BECs 24 h post-transfection with miR-383-3p-sEVs or miR-scr-sEVs. Scale bar is $20 \mu\text{m}$. **j** Mean claudin 5 expression per cell. **l** Mean vWF expression per cell. In **j** and **l** results are mean \pm SEM ($n=3$ independent experiments, with 3–5 images analyzed for each condition). Unpaired *t*-test was performed, $*p < 0.05$ and $***p < 0.001$

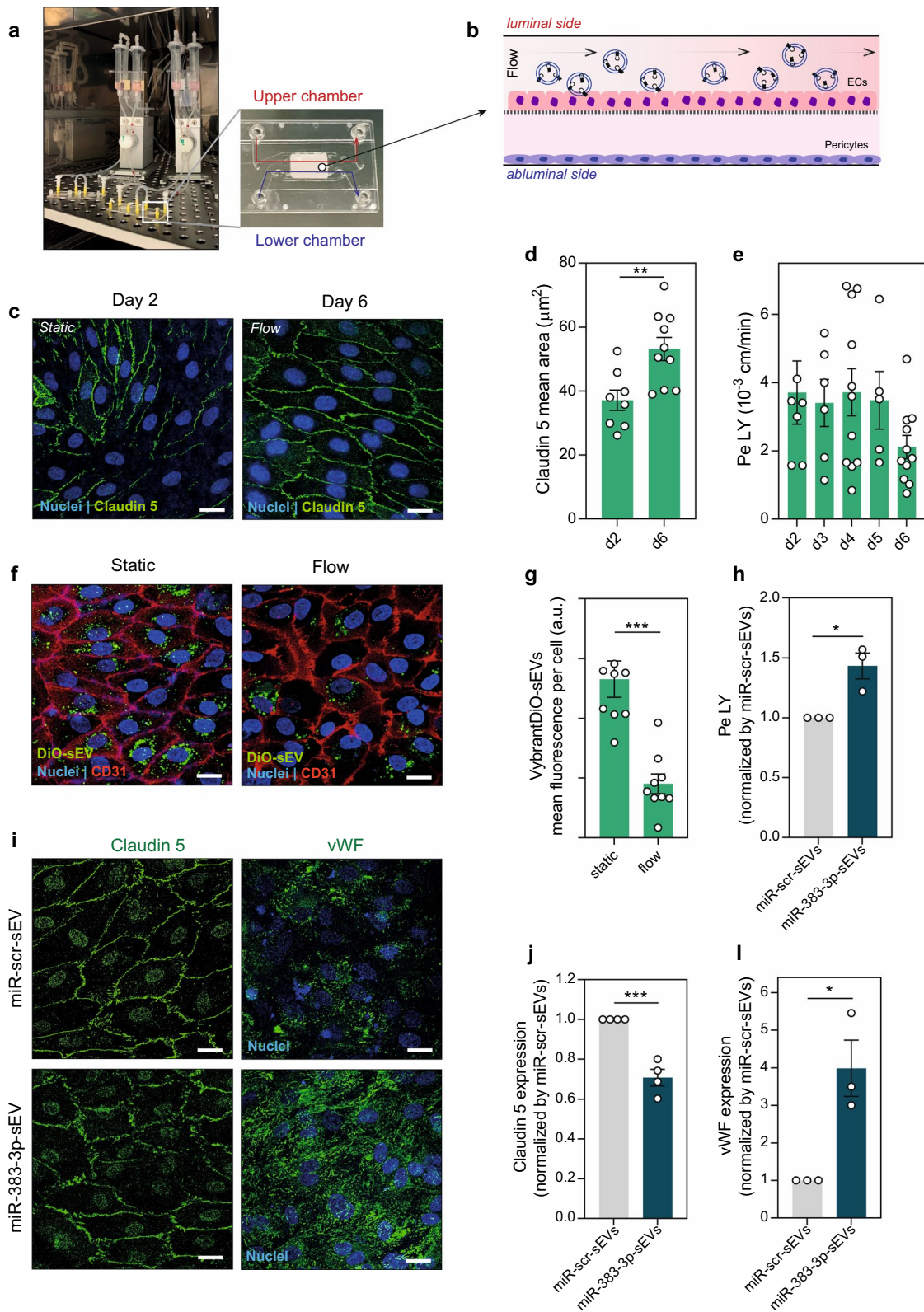


Fig. 7 (See legend on previous page.)

be observed with “old” sEVs. We established a blood–brain barrier (BBB) in a microfluidic system over 6 days, perfused the model with “old” sEVs at a concentration of 10^{10} sEVs/mL for 48 h and then evaluated its paracellular permeability to LY. Our results showed a fourfold increase in permeability to LY (Additional file 1: Figure S8a) and a decrease in claudin-5 expression compared to the non-treated BBB model (Additional file 1: Figure S8b, c).

Altogether, these results allowed us to confirm that the miR-383-3p-sEVs can induce the BBB opening also in a more relevant in vitro BBB model.

Discussion

The current study demonstrates, by using two human in vitro BBB models, the capacity of human plasma sEVs enriched with miR-383-3p, a miRNA connected with aging, to transiently open the BBB. The temporary opening was mediated by the knockdown of *ATF4* transcription factor, and the mineralocorticoid receptor encoded by *NR3C2* gene which then induced a decrease in claudin 5 expression. The current formulation can be seen as an alternative to the current strategies to transiently open the BBB.

The BBB integrity is controlled by junction complexes composed by TJs and adherens junctions (AJs) [120]. The AJs mainly consist of cadherins [120]. The TJs include claudins (e.g., claudin 1, claudin 2, claudin 3, claudin 5, etc.), occludin, junction adhesion molecules (JAMs) and cytoplasmic accessory proteins (e.g., zonula occludens-1 (ZO-1), ZO-2, ZO-3, etc.). The expression patterns of claudins vary significantly among different tissue barriers. In the gut barrier, the predominant claudins include claudin-2, claudin-3, claudin-7, claudin-15 [121], and claudin-23 [122]. In the colon, claudin-1, claudin-3, and claudin-7 are more highly expressed [123]. Similarly, in the respiratory tree, claudin-4, claudin-7, and claudin-18 are the main claudins present [124]. The most abundant claudin in BECs is claudin 5. This claudin plays an important role in the maintenance of BBB integrity since claudin 5 knockout mice show increased BBB permeability [125]. Claudin 5 expression is regulated by several upstream signaling pathways at the transcriptional levels including VEGF signaling [126]. Importantly, ATF4 regulates the expression of VEGF, i.e., a downregulation in the expression of ATF4 leads to an upregulation of VEGF [127]. To the best of our knowledge, this signaling pathway has not been previously reported to regulate BBB opening.

MicroRNAs are a class of short non-coding RNAs which expression in the blood plasma is affected during aging, regulating the integrity of biological barriers,

including the BBB. We have monitored the expression of several miRNAs that are upregulated in aging, age-related diseases and senescence in plasma, blood, and circulating EVs. Our results showed for the first time a significant increase in the expression of miR-383-3p in the circulating sEVs during physiological aging. Until now, the upregulation of miR-383-3p had been reported in the context of age-related diseases such as skin photoaging [128], or in the context of ischemia by middle cerebral artery occlusion [67], but not during physiological aging. Our results further show that miR-383-3p regulates ATF4 expression. This transcription factor is reported to be activated by the unfolded protein response [129], by starvation [130], and by oxidized phospholipids [131]. In particular, it is reported to play a pro-angiogenic role [132–134], together with VEGF [130–132, 134]. A link between miR-383-3p and ATF4 has been documented before in the crosstalk between microglia cells and neurons [48] but not in the context of the BBB. Claudin 5 is not a direct target of miR-383-3p due to the absence of reduction in the gene expression, however the indirect effect of miR-383-3p on reducing claudin 5 may account for the increase in the paracellular permeability. Immunocytochemistry showed a decreased intensity signal for claudin 5 in *ATF4* siRNA transfected BECs (Fig. 6d) suggesting that miR-383-3p-sEVs effect on claudin 5 may be partially mediated by the knockdown of the *ATF4*. Because miR-383-3p knocks down ATF4, we cannot exclude the possibility that miR-383-3p-sEVs might affect other biological barriers; however, it is important to note that claudin-5, an indirect target of miR-383-3p is mostly expressed in brain endothelial cells at the BBB. In addition, miR-383-3p-sEVs can be conjugated at the membrane surface with antibodies or peptides targeting more specifically the BBB [19].

Our results show that sEVs can be used to deliver miRNAs within BECs and regulate the permeability of the BBB. Previous studies showed that sEVs are involved in many processes related with aging and are able to cross the BBB [44]. The content of the EVs has been reported to change with age [58, 135, 136], especially in terms of miRNA content [59, 137]. Therefore, sEVs collected from a young biological fluid (UCB plasma) were enriched with miRNAs associated with aging to develop a formulation able to reversibly open the BBB. We were able to successfully enrich sEVs content with a miRNA of interest (both compared to native young and old sEVs) without altering significantly their morphological characteristics and cellular uptake in comparison to native sEVs. Incubation of a human in vitro BBB model with different concentrations of sEVs, showed that the vesicles alone did not impair BBB function; however, when the incubation was done with miR-383-3p-sEVs there was an increase

in the paracellular permeability to LY compared to the miR-scr-sEVs. A previous study has shown that miR-34a-5p induced an increase of BBB permeability when overexpressed in murine BECs used for the BBB model [88]; however, we could not replicate those results in our human model. It is possible that differences in BECs may explain these discrepancies.

Our study demonstrates in two human in vitro BBB models the capacity of human plasma sEVs enriched with miR-383-3p to transiently open the BBB. We used a microfluidic chip to co-culture human BECs (cultured in the top compartment, with flow) with human pericytes (cultured in the low compartment) simulating the shear stress that the cells sense in the microvasculature [116]. We confirmed a BEC monolayer formation with the TJs protein claudin 5 present in the cell membrane and fully organized at day 6. Despite the lower uptake of sEVs enriched with miR-383-3p in flow *versus* static conditions, likely due to a limited interaction of sEVs with BEC membrane, the paracellular permeability of the BBB model increased at expenses of a downregulation in claudin 5 protein expression. To our knowledge, this is the first study using engineered sEVs in a microfluidic system to modulate a human BBB model.

An important feature of the strategy to open the BBB is the reversibility of the effects. Our results show that the BBB model transfected with miR-383-3p-sEVs recover the BBB paracellular permeability 24 h after removing the sEVs. At this time point, there was not significant difference between the BBB treated with miR-scr-sEVs (scramble) and with miR-383-3p-sEVs. Also, claudin 5 expression increased again in the condition incubated with miR-383-3p-sEVs 24 h after the removal of the vesicles from the BBB model. Our results suggest that miR-383-3p-sEVs-induced decrease of BBB permeability may be partially mediated by an increase of claudin 5 at protein level.

Conclusions

In conclusion, we took inspiration from the aging processes to develop a new strategy to temporarily open the BBB. Plasma sEVs enriched with miR-383-3p may be an alternative to the others being investigated at pre-clinical and clinical levels to transiently control the BBB permeability. Moreover, we describe for the first time the impact of human modulated sEVs in a human BBB model.

Abbreviations

BBB	Blood–brain barrier
sEVs	Small extracellular vesicles
miRNA	MicroRNA
ATF4	Activating transcription factor 4
ECs	Endothelial cells
BECs	Brain endothelial cells
NVU	Neurovascular unit

TJs	Tight junctions
UCB	Umbilical cord blood
PBS	Phosphate-buffered saline
ODG	Optiprep density gradient
DLS	Dynamic light scattering
NTA	Nanoparticle tracking analysis
TEM	Transmission electron microscopy
RT-qPCR	Reverse transcription quantitative polymerase chain reaction
PFA	Paraformaldehyde
PLL	Poly-L-lysine
HBVP	Human brain vascular pericytes
RT	Room temperature
Pe	Paracellular permeability

Supplementary Information

The online version contains supplementary material available at <https://doi.org/10.1186/s12951-024-03019-w>.

Additional file 1.
Additional file 2.
Additional file 3.
Additional file 4.
Additional file 5.

Acknowledgements

The authors would like to acknowledge the funding from the European Commission through the Marie Skłodowska-Curie Innovative Training Network “NANOSTEM” (ref. 764958) and twinning RESEAgeing project (ref. 952266); the Portuguese funding research institution (FCT) for the funding through the projects PTDC/BTM-SAL/5174/2020, 2022.07615.PTDC, 2022.02803.PTDC, EXCAVATOR project (2023.15026.PEX); and the PRR project HfPT- Health from Portugal (ref. 02/C05-i01.01/2022.PC644937233-00000047). FT would like also to acknowledge the FCT fellowship entitled “Polymeric nanoparticles loaded with CRISPR/dCas9 for direct cell reprogramming” (n. 2021.06297.BD) CJ acknowledge for FCT fellowship SFRH/BD/144092/2019 and MB acknowledge for FCT fellowship n. 2020.09432.BD. SR acknowledge to FCT for the funding DL 57/2016/CP1448/CT0018 and SS for the FCT funding DL 57/2016/CP1448/CT0010.

Author contributions

FT, SR, SS, LF conceived the experiments and interpreted the data; FT, SR, CJ and JN performed the experiments; EB and MM looked for the direct targets of the miR-383-3p; MB helped in performing the western blot experiments; FT wrote the paper; SR, SS, LF reviewed and edited the manuscript. All authors read and approved the final manuscript.

Funding

The authors would like to express their gratitude to the European Commission for the funding through the Marie Skłodowska-Curie Innovative Training Network “NANOSTEM” (n. 764958) and to FCT for the funding through the projects PTDC/BTM-SAL/5174/2020, 2022.07615.PTDC, EXCAVATOR project (2023.15026.PEX); and the fellowship SFRH/BD/144092/2019, 2020.09432.BD, 2021.04579.BD and 2021.06297.BD. SR acknowledge to FCT for the funding DL 57/2016/CP1448/CT0018 and SS for the FCT funding DL 57/2016/CP1448/CT0010.

Availability of data and materials

No datasets were generated or analysed during the current study.

Declarations

Ethics approval and consent to participate

The collection of umbilical cord blood (UCB) was approved by the ethical committee of Dr. Daniel de Matos Maternity Hospital in Coimbra (protocol HUC-01-11), Portugal. The collection of adult blood was approved by the Faculty of Medicine of the University of Coimbra and the Portuguese Institute

for Blood and Transplantation (IPST) in the facilities of Blood and Transplantation Center of Coimbra (CSTC) (protocol: CE-088/2020). All the donors of the UCB and adult blood signed an informed consent form, in compliance with the Portuguese legislation.

Consent for publication

Not applicable.

Competing interests

The authors declare no competing interests.

Author details

¹CNC-UC - Center for Neuroscience and Cell Biology, University of Coimbra, UC—Biotech Parque Tecnológico de Cantanhede, Coimbra, Portugal. ²CIBB - Centre for Innovative Biomedicine and Biotechnology, University of Coimbra, UC—Biotech Parque Tecnológico de Cantanhede, Coimbra, Portugal. ³Doctoral Programme in Experimental Biology and Biomedicine (PDBEB), Institute for Interdisciplinary Research, University of Coimbra, Coimbra, Portugal. ⁴Bioinformatics Core Facility, Faculty of Mathematics and Computer Science, Friedrich Schiller University Jena, Jena, Germany. ⁵Bioinformatics/High Throughput Analysis, Faculty of Mathematics and Computer Science, Friedrich Schiller University Jena, Jena, Germany. ⁶FLI Leibniz Institute for Age Research, Jena, Germany. ⁷German Center for Integrative Biodiversity Research (iDiv), Halle-Jena-Leipzig, Germany. ⁸European Virus Bioinformatics Center (EVBC), Jena, Germany. ⁹Faculty of Medicine, University of Coimbra, Coimbra, Portugal.

Received: 31 May 2024 Accepted: 14 November 2024

Published online: 02 December 2024

References

- Sweeney MD, et al. Blood–brain barrier: from physiology to disease and back. *Physiol Rev*. 2019;99(1):21–78.
- Engelhardt B, Sorokin L. The blood–brain and the blood–cerebrospinal fluid barriers: function and dysfunction. *Semin Immunopathol*. 2009;31(4):497–511.
- Cui Y, et al. Brain endothelial PTEN/AKT/NEDD4-2/MFSD2A axis regulates blood–brain barrier permeability. *Cell Rep*. 2021;36(1): 109327.
- Oldendorf WH, Brown WJ. Greater number of capillary endothelial cell mitochondria in brain than in muscle. *Proc Soc Exp Biol Med*. 1975;149(3):736–8.
- Lipinski CA. Drug-like properties and the causes of poor solubility and poor permeability. *J Pharmacol Toxicol Methods*. 2000;44(1):235–49.
- Pardridge WM. Drug targeting to the brain. *Pharm Res*. 2007;24(9):1733–44.
- Choudhari M, et al. Evolving new-age strategies to transport therapeutics across the blood–brain–barrier. *Int J Pharm*. 2021;599: 120351.
- Cosolo WC, et al. Blood–brain barrier disruption using mannitol: time course and electron microscopy studies. *Am J Physiol*. 1989;256(2 Pt 2):R443–7.
- Bellavance MA, Blanchette M, Fortin D. Recent advances in blood–brain barrier disruption as a CNS delivery strategy. *AAPS J*. 2008;10(1):166–77.
- Del Vecchio G, et al. Sodium caprate transiently opens claudin-5-containing barriers at tight junctions of epithelial and endothelial cells. *Mol Pharm*. 2012;9(9):2523–33.
- Boye K, et al. Endothelial Unc5B controls blood–brain barrier integrity. *Nat Commun*. 2022;13(1):1169.
- Villalba N, et al. Site-specific opening of the blood–brain barrier by extracellular histones. *J Neuroinflammation*. 2020;17(1):281.
- Kim DG, et al. Gintonin, a ginseng-derived exogenous lysophosphatidic acid receptor ligand, enhances blood–brain barrier permeability and brain delivery. *Int J Biol Macromol*. 2018;114:1325–37.
- Bartus RT, et al. Controlled modulation of BBB permeability using the bradykinin agonist, RMP-7. *Exp Neurol*. 1996;142(1):14–28.
- Alonso A. Ultrasound-induced blood–brain barrier opening for drug delivery. *Front Neurol Neurosci*. 2015;36:106–15.
- Tung YS, et al. The mechanism of interaction between focused ultrasound and microbubbles in blood–brain barrier opening in mice. *J Acoust Soc Am*. 2011;130(5):3059–67.
- Ashraf O, et al. Laser-induced thermal therapy in neuro-oncology: a review. *World Neurosurg*. 2018;112:166–77.
- Li X, et al. Reversibly modulating the blood–brain barrier by laser stimulation of molecular-targeted nanoparticles. *Nano Lett*. 2021;21(22):9805–15.
- Praca C, et al. A nanoformulation for the preferential accumulation in adult neurogenic niches. *J Control Release*. 2018;284:57–72.
- Bouchet A, et al. Permeability of brain tumor vessels induced by uniform or spatially microfractionated synchrotron radiation therapies. *Int J Radiat Oncol Biol Phys*. 2017;98(5):1174–82.
- Furtado D, et al. Overcoming the blood–brain barrier: the role of nanomaterials in treating neurological diseases. *Adv Mater*. 2018;30(46): e1801362.
- Seo S, et al. Triculture model of in vitro BBB and its application to study BBB-associated chemosensitivity and drug delivery in glioblastoma. *Adv Funct Mater*. 2022;32(10):2106860.
- Neuwelt EA, et al. Reversible osmotic blood–brain barrier disruption in humans: implications for the chemotherapy of malignant brain tumors. *Neurosurgery*. 1980;7(1):44–52.
- Rapoport SI. Osmotic opening of the blood–brain barrier: principles, mechanism, and therapeutic applications. *Cell Mol Neurobiol*. 2000;20(2):217–30.
- Burks SR, et al. Blood–brain barrier opening by intracarotid artery hyperosmolar mannitol induces sterile inflammatory and innate immune responses. *Proc Natl Acad Sci*. 2021;118(18):e2021915118.
- Abraham A, et al. First-in-human trial of blood–brain barrier opening in amyotrophic lateral sclerosis using MR-guided focused ultrasound. *Nat Commun*. 2019;10(1):4373.
- Rezai AR, et al. Noninvasive hippocampal blood–brain barrier opening in Alzheimer’s disease with focused ultrasound. *Proc Natl Acad Sci U S A*. 2020;117(17):9180–2.
- Kovacs ZI, et al. Disrupting the blood–brain barrier by focused ultrasound induces sterile inflammation. *Proc Natl Acad Sci U S A*. 2017;114(1):E75–84.
- Jung O, et al. Neuroinflammation associated with ultrasound-mediated permeabilization of the blood–brain barrier. *Trends Neurosci*. 2022;45(6):459–70.
- Hashimoto Y, Campbell M. Tight junction modulation at the blood–brain barrier: current and future perspectives. *Biochim Biophys Acta Biomembr*. 2020;1862(9): 183298.
- Wala K, Szlasa W, Saczko J, Rudno-Rudzińska J, Kulbacka J. Modulation of blood–brain barrier permeability by activating adenosine A2 receptors in oncological treatment. *Biomolecules*. 2021;11(5):633.
- Carman AJ, et al. Adenosine receptor signaling modulates permeability of the blood–brain barrier. *J Neurosci*. 2011;31(37):13272–80.
- Jackson S, et al. The effect of an adenosine A(2A) agonist on intratumoral concentrations of temozolomide in patients with recurrent glioblastoma. *Fluids Barriers CNS*. 2018;15(1):2.
- Verheggen ICM, et al. Increase in blood–brain barrier leakage in healthy, older adults. *Geroscience*. 2020;42(4):1183–93.
- Montagne A, et al. Blood–brain barrier breakdown in the aging human hippocampus. *Neuron*. 2015;85(2):296–302.
- Yang AC, et al. Physiological blood–brain transport is impaired with age by a shift in transcytosis. *Nature*. 2020;583(7816):425–30.
- Galea I. The blood–brain barrier in systemic infection and inflammation. *Cell Mol Immunol*. 2021;18(11):2489–501.
- Villeda SA, et al. Young blood reverses age-related impairments in cognitive function and synaptic plasticity in mice. *Nat Med*. 2014;20(6):659–63.
- Villeda SA, et al. The ageing systemic milieu negatively regulates neurogenesis and cognitive function. *Nature*. 2011;477(7362):90–4.
- Busatto S, et al. The role of extracellular vesicles in the physiological and pathological regulation of the blood–brain barrier. *FASEB Bioadv*. 2021;3(9):665–75.
- Lino MM, et al. Engineered extracellular vesicles as brain therapeutics. *J Control Release*. 2021;338:472–85.
- van Niel G, D’Angelo G, Raposo G. Shedding light on the cell biology of extracellular vesicles. *Nat Rev Mol Cell Biol*. 2018;19(4):213–28.
- de Abreu RC, et al. Native and bioengineered extracellular vesicles for cardiovascular therapeutics. *Nat Rev Cardiol*. 2020;17(11):685–97.

44. Morales-Prieto DM, et al. Small extracellular vesicles from peripheral blood of aged mice pass the blood-brain barrier and induce glial cell activation. *Cells*. 2022;11(4):625.
45. de Abreu RC, et al. Exogenous loading of miRNAs into small extracellular vesicles. *J Extracell Vesicles*. 2021;10(10): e12111.
46. Cecchelli R, et al. A stable and reproducible human blood-brain barrier model derived from hematopoietic stem cells. *PLoS ONE*. 2014;9(6): e99733.
47. Van Deun J, et al. The impact of disparate isolation methods for extracellular vesicles on downstream RNA profiling. *J Extracell Vesicles*. 2014;3(1):24858.
48. Wei M, et al. Activated microglia exosomes mediated miR-383-3p promotes neuronal necroptosis through inhibiting ATF4 expression in intracerebral hemorrhage. *Neurochem Res*. 2021;46(6):1337–49.
49. Zeng H, et al. Overexpression of miR-383-3p protects cardiomyocytes against hypoxia/reoxygenation injury via regulating PTEN/PI3K/AKT signal pathway. *J Biochem Mol Toxicol*. 2022;36(12): e23205.
50. Nossent AY, et al. SNPs in microRNA binding sites in 3'-UTRs of RAAS genes influence arterial blood pressure and risk of myocardial infarction. *Am J Hypertens*. 2011;24(9):999–1006.
51. Fehlmann T, et al. Common diseases alter the physiological age-related blood microRNA profile. *Nat Commun*. 2020;11(1):5958.
52. Mensa E, et al. Small extracellular vesicles deliver miR-21 and miR-217 as pro-senescence effectors to endothelial cells. *J Extracell Vesicles*. 2020;9(1):1725285.
53. Huan T, et al. Age-associated micro RNA expression in human peripheral blood is associated with all-cause mortality and age-related traits. *Aging Cell*. 2018;17(1):e12687.
54. Zhang H, et al. Investigation of microRNA expression in human serum during the aging process. *J Gerontol A Biol Sci Med Sci*. 2015;70(1):102–9.
55. Meder B, et al. Influence of the confounding factors age and sex on microRNA profiles from peripheral blood. *Clin Chem*. 2014;60(9):1200–8.
56. Olivieri F, et al. Age-related differences in the expression of circulating microRNAs: miR-21 as a new circulating marker of inflammaging. *Mech Ageing Dev*. 2012;133(11–12):675–85.
57. ElSharawy A, et al. Genome-wide miRNA signatures of human longevity. *Aging Cell*. 2012;11(4):607–16.
58. Alibhai FJ, et al. Cellular senescence contributes to age-dependent changes in circulating extracellular vesicle cargo and function. *Aging Cell*. 2020;19(3): e13103.
59. Tsukamoto H, Kouwaki T, Oshiumi H. Aging-associated extracellular vesicles contain immune regulatory microRNAs alleviating hyperinflammatory state and immune dysfunction in the elderly. *Iscience*. 2020;23(9):101520.
60. Fulzele S, et al. Muscle-derived miR-34a increases with age in circulating extracellular vesicles and induces senescence of bone marrow stem cells. *Aging (Albany NY)*. 2019;11(6):1791–803.
61. Raucci A, et al. MicroRNA-34a: the bad guy in age-related vascular diseases. *Cell Mol Life Sci*. 2021;78(23):7355–78.
62. Rani A, et al. miRNA in circulating microvesicles as biomarkers for age-related cognitive decline. *Front Aging Neurosci*. 2017;9:323.
63. Carini G, et al. miRNome profiling detects miR-101-3p and miR-142-5p as putative blood biomarkers of frailty syndrome. *Genes*. 2022;13(2):231.
64. Zhang M, et al. miR-101-3p contributes to alpha-synuclein aggregation in neural cells through the miR-101-3p/SKP1/PLK2 pathway. *J Healthc Eng*. 2021;2021:6147434.
65. Zhao J, He Z, Wang J. MicroRNA-124: a key player in microglia-mediated inflammation in neurological diseases. *Front Cell Neurosci*. 2021;15: 771898.
66. Guevremont D, et al. Plasma microRNA vary in association with the progression of Alzheimer's disease. *Alzheimers Dement (Amst)*. 2022;14(1): e12251.
67. Jeyaseelan K, Lim KY, Armugam A. MicroRNA expression in the blood and brain of rats subjected to transient focal ischemia by middle cerebral artery occlusion. *Stroke*. 2008;39(3):959–66.
68. Dimmeler S, Nicotera P. MicroRNAs in age-related diseases. *EMBO Mol Med*. 2013;5(2):180–90.
69. Ryu IS, et al. The role of microRNA-485 in neurodegenerative diseases. *Rev Neurosci*. 2023;34(1):49–62.
70. Zhang YH, Bai SF, Yan JQ. Blood circulating miRNAs as biomarkers of Alzheimer's disease: a systematic review and meta-analysis. *Biomark Med*. 2019;13(12):1045–54.
71. Uwatoko H, et al. Identification of plasma microRNA expression changes in multiple system atrophy and Parkinson's disease. *Mol Brain*. 2019;12(1):49.
72. Kumar S, et al. MicroRNAs as peripheral biomarkers in aging and age-related diseases. *Prog Mol Biol Transl Sci*. 2017;146:47–94.
73. Ma J, et al. Knockdown of long non-coding RNA MALAT1 increases the blood-tumor barrier permeability by up-regulating miR-140. *Biochim Biophys Acta*. 2016;1859(2):324–38.
74. Mishra R, Singh SK. HIV-1 Tat C modulates expression of miRNA-101 to suppress VE-cadherin in human brain microvascular endothelial cells. *J Neurosci*. 2013;33(14):5992–6000.
75. Wang Y, et al. MicroRNA-130a regulates cerebral ischemia-induced blood-brain barrier permeability by targeting Homeobox A5. *FASEB J*. 2018;32(2):935–44.
76. Yu H, et al. Knockdown of long non-coding RNA XIST increases blood-tumor barrier permeability and inhibits glioma angiogenesis by targeting miR-137. *Oncogenesis*. 2017;6(3): e303.
77. Bai Y, et al. Silencing microRNA-143 protects the integrity of the blood-brain barrier: implications for methamphetamine abuse. *Sci Rep*. 2016;6:35642.
78. Cai H, et al. The long noncoding RNA TUG1 regulates blood-tumor barrier permeability by targeting miR-144. *Oncotarget*. 2015;6(23):19759–79.
79. Fang Z, et al. MicroRNA-150 regulates blood-brain barrier permeability via Tie-2 after permanent middle cerebral artery occlusion in rats. *FASEB J*. 2016;30(6):2097–107.
80. Pena-Philippides JC, Gardiner AS, Caballero-Garrido E, Pan R, Zhu Y, Roitbak T. Inhibition of MicroRNA-155 supports endothelial tight junction integrity following oxygen-glucose deprivation. *J Am Heart Assoc*. 2018;7(13):e009244.
81. Lopez-Ramirez MA, et al. MicroRNA-155 negatively affects blood-brain barrier function during neuroinflammation. *FASEB J*. 2014;28(6):2551–65.
82. Barker KR, et al. miR-155 modifies inflammation, endothelial activation and blood-brain barrier dysfunction in cerebral malaria. *Mol Med*. 2017;23:24–33.
83. Ma J, et al. MiR-181a regulates blood-tumor barrier permeability by targeting Kruppel-like factor 6. *J Cereb Blood Flow Metab*. 2014;34(11):1826–36.
84. Tominaga N, et al. Brain metastatic cancer cells release microRNA-181c-containing extracellular vesicles capable of destructing blood-brain barrier. *Nat Commun*. 2015;6:6716.
85. Guo J, et al. Long non-coding RNA NEAT1 regulates permeability of the blood-tumor barrier via miR-181d-5p-mediated expression changes in ZO-1, occludin, and claudin-5. *Biochim Biophys Acta Mol Basis Dis*. 2017;1863(9):2240–54.
86. Miao YS, et al. MiR-18a increased the permeability of BTB via RUNX1 mediated down-regulation of ZO-1, occludin and claudin-5. *Cell Signal*. 2015;27(1):156–67.
87. Kalani A, et al. Role of microRNA29b in blood-brain barrier dysfunction during hyperhomocysteinemia: an epigenetic mechanism. *J Cereb Blood Flow Metab*. 2014;34(7):1212–22.
88. Bukeirat M, et al. MiR-34a regulates blood-brain barrier permeability and mitochondrial function by targeting cytochrome c. *J Cereb Blood Flow Metab*. 2016;36(2):387–92.
89. Zhao W, et al. MiR-34a regulates blood-tumor barrier function by targeting protein kinase Cepsilon. *Mol Biol Cell*. 2015;26(10):1786–96.
90. Zhao L, et al. miR-34c regulates the permeability of blood-tumor barrier via MAZ-mediated expression changes of ZO-1, occludin, and claudin-5. *J Cell Physiol*. 2015;230(3):716–31.
91. Chu Y, et al. Tetrandrine attenuates intestinal epithelial barrier defects caused by colitis through promoting the expression of Occludin via the AhR-miR-429 pathway. *FASEB J*. 2021;35(5): e21502.
92. Toyama K, et al. MicroRNA-mediated therapy modulating blood-brain barrier disruption improves vascular cognitive impairment. *Arterioscler Thromb Vasc Biol*. 2018;38(6):1392–406.

93. Leng X, et al. Mechanism of piR-DQ590027/MIR17HG regulating the permeability of glioma conditioned normal BBB. *J Exp Clin Cancer Res.* 2018;37(1):246.
94. Zhang W, et al. Exosomal miR-22-3p derived from chronic rhinosinusitis with nasal polyps regulates vascular permeability by targeting VE-cadherin. *Biomed Res Int.* 2020;2020:1237678.
95. Matsuoka H, et al. Levels of tight junction protein CLDN1 are regulated by microRNA-124 in the cerebellum of stroke-prone spontaneously hypertensive rats. *Biochem Biophys Res Commun.* 2018;498(4):817–23.
96. Gu W, et al. MicroRNA-22 regulates inflammation and angiogenesis via targeting VE-cadherin. *FEBS Lett.* 2017;591(3):513–26.
97. Xu B, et al. Neurons secrete miR-132-containing exosomes to regulate brain vascular integrity. *Cell Res.* 2017;27(7):882–97.
98. Burek M, et al. Hypoxia-induced microRNA-212/132 alter blood–brain barrier integrity through inhibition of tight junction-associated proteins in human and mouse brain microvascular endothelial cells. *Transl Stroke Res.* 2019;10(6):672–83.
99. Pei L, et al. Inhibition of MicroRNA-383 ameliorates injury after focal cerebral ischemia via targeting PPARgamma. *Cell Physiol Biochem.* 2016;39(4):1339–46.
100. Lin M, et al. miR-424-5p maybe regulate blood–brain barrier permeability in a model in vitro with Abeta incubated endothelial cells. *Biochem Biophys Res Commun.* 2019;517(3):525–31.
101. Ma F, Zhang X, Yin KJ. MicroRNAs in central nervous system diseases: a prospective role in regulating blood–brain barrier integrity. *Exp Neurol.* 2020;323: 113094.
102. Zhou W, et al. Cancer-secreted miR-105 destroys vascular endothelial barriers to promote metastasis. *Cancer Cell.* 2014;25(4):501–15.
103. Muramatsu F, et al. microRNA-125b inhibits tube formation of blood vessels through translational suppression of VE-cadherin. *Oncogene.* 2013;32(4):414–21.
104. Lalwani MK, et al. Reverse genetics screen in zebrafish identifies a role of miR-142a-3p in vascular development and integrity. *PLoS ONE.* 2012;7(12): e52588.
105. Young JA, et al. Regulation of vascular leak and recovery from ischemic injury by general and VE-cadherin-restricted miRNA antagonists of miR-27. *Blood.* 2013;122(16):2911–9.
106. Zhu K, et al. MiR-302c inhibits tumor growth of hepatocellular carcinoma by suppressing the endothelial–mesenchymal transition of endothelial cells. *Sci Rep.* 2014;4:5524.
107. Wang Y, et al. Regulation of proliferation, angiogenesis and apoptosis in hepatocellular carcinoma by miR-26b-5p. *Tumour Biol.* 2016;37(8):10965–79.
108. Chen L, et al. VHL regulates the effects of miR-23b on glioma survival and invasion via suppression of HIF-1alpha/VEGF and beta-catenin/Tcf-4 signaling. *Neuro Oncol.* 2012;14(8):1026–36.
109. Toyama K, Spin JM, Tsao PS. Role of microRNAs on blood brain barrier dysfunction in vascular cognitive impairment. *Curr Drug Deliv.* 2017;14(6):744–57.
110. Jakubec M, et al. Plasma-derived exosome-like vesicles are enriched in lyso-phospholipids and pass the blood-brain barrier. *PLoS ONE.* 2020;15(9):e0232442.
111. Saleh AF, et al. Extracellular vesicles induce minimal hepatotoxicity and immunogenicity. *Nanoscale.* 2019;11(14):6990–7001.
112. Welsh JA, et al. Minimal information for studies of extracellular vesicles (MISEV2023): from basic to advanced approaches. *J Extracell Vesicles.* 2024;13(2):e12404.
113. Suidan GL, et al. Endothelial Von Willebrand factor promotes blood–brain barrier flexibility and provides protection from hypoxia and seizures in mice. *Arterioscler Thromb Vasc Biol.* 2013;33(9):2112–20.
114. Hajal C, et al. Engineered human blood–brain barrier microfluidic model for vascular permeability analyses. *Nat Protoc.* 2022;17(1):95–128.
115. Cucullo L, et al. Immortalized human brain endothelial cells and flow-based vascular modeling: a marriage of convenience for rational neurovascular studies. *J Cereb Blood Flow Metab.* 2008;28(2):312–28.
116. Cucullo L, et al. The role of shear stress in blood–brain barrier endothelial physiology. *BMC Neurosci.* 2011;12:40.
117. Kurokawa YK, et al. Human induced pluripotent stem cell-derived endothelial cells for three-dimensional microphysiological systems. *Tissue Eng Part C Methods.* 2017;23(8):474–84.
118. Vatine GD, et al. Human iPSC-derived blood-brain barrier chips enable disease modeling and personalized medicine applications. *Cell Stem Cell.* 2019;24(6):995–1005.
119. Morad G, et al. Tumor-derived extracellular vesicles breach the intact blood–brain barrier via transcytosis. *ACS Nano.* 2019;13(12):13853–65.
120. Aday S, et al. Stem cell-based human blood–brain barrier models for drug discovery and delivery. *Trends Biotechnol.* 2016;34(5):382–93.
121. Lu Z, et al. Claudins in intestines: distribution and functional significance in health and diseases. *Tissue Barriers.* 2013;1(3): e24978.
122. Raya-Sandino A, et al. Claudin-23 reshapes epithelial tight junction architecture to regulate barrier function. *Nat Commun.* 2023;14(1):6214.
123. Cox KE, et al. The expression of the Claudin family of proteins in colorectal cancer. *Biomolecules.* 2024;14(3):272.
124. Schlingmann B, Molina SA, Koval M. Claudins: Gatekeepers of lung epithelial function. *Semin Cell Dev Biol.* 2015;42:47–57.
125. Nitta T, et al. Size-selective loosening of the blood–brain barrier in claudin-5-deficient mice. *J Cell Biol.* 2003;161(3):653–60.
126. Greene C, Hanley N, Campbell M. Claudin-5: gatekeeper of neurological function. *Fluids Barriers CNS.* 2019;16(1):3.
127. Neill G, Masson GR. A stay of execution: ATF4 regulation and potential outcomes for the integrated stress response. *Front Mol Neurosci.* 2023;16:112253.
128. Gerasymchuk M, et al. The role of microRNAs in organismal and skin aging. *Int J Mol Sci.* 2020;21(15):5281.
129. Petry A, et al. Cross talk between p22phox and ATF4 in the endothelial unfolded protein response. *Antioxid Redox Signal.* 2019;30(1):40–55.
130. Puschel F, et al. Starvation and antimetabolic therapy promote cytokine release and recruitment of immune cells. *Proc Natl Acad Sci U S A.* 2020;117(18):9932–41.
131. Afonyushkin T, et al. Oxidized phospholipids regulate expression of ATF4 and VEGF in endothelial cells via NRF2-dependent mechanism: novel point of convergence between electrophilic and unfolded protein stress pathways. *Arterioscler Thromb Vasc Biol.* 2010;30(5):1007–13.
132. Chen L, et al. Activating transcription factor 4 regulates angiogenesis under lipid overload via methionine adenosyltransferase 2A-mediated endothelial epigenetic alteration. *FASEB J.* 2021;35(6): e21612.
133. Fan Z, et al. Exercise-induced angiogenesis is dependent on metabolically primed ATF3/4+ endothelial cells. *Cell Metab.* 2021;33(9):1793–807.
134. Yasuda H, et al. Role of activating transcription factor 4 in murine chorioidal neovascularization model. *Int J Mol Sci.* 2021;22(16).
135. Noren Hooten N, et al. Influences of age, race, and sex on extracellular vesicle characteristics. *Theranostics.* 2022;12(9):4459–76.
136. Eitan E, et al. Age-related changes in plasma extracellular vesicle characteristics and internalization by leukocytes. *Sci Rep.* 2017;7(1):1342.
137. Zhang Y, et al. Hypothalamic stem cells control ageing speed partly through exosomal miRNAs. *Nature.* 2017;548(7665):52–7.

Publisher's Note

Springer Nature remains neutral with regard to jurisdictional claims in published maps and institutional affiliations.